RICE UNIVERSITY

Direct plasmon-driven photoelectrocatalysis

by

Hossein Robatjazi

A THESIS SUBMITTED
IN PARTIAL FULFILLMENT OF THE
REQUIREMENTS FOR THE DEGREE

Master of Science

APPROVED, THESIS COMMITTEE

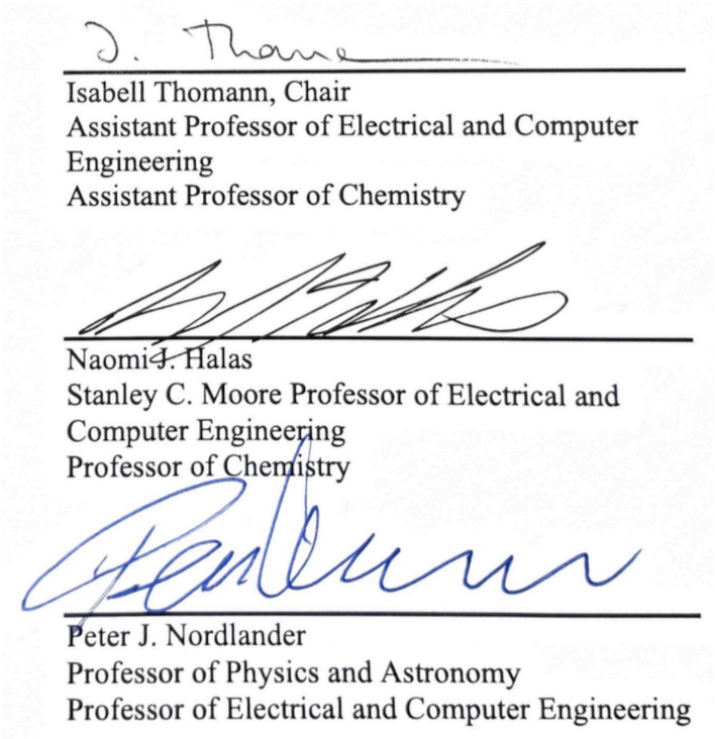

Isabell Thomann, Chair
Assistant Professor of Electrical and Computer Engineering
Assistant Professor of Chemistry

Naomi J. Halas
Stanley C. Moore Professor of Electrical and Computer Engineering
Professor of Chemistry

Peter J. Nordlander
Professor of Physics and Astronomy
Professor of Electrical and Computer Engineering

HOUSTON, TX
May 2016

Abstract

Direct Plasmon-driven photoelectrocatalysis

by

Hossein Robatjazi

Harnessing the energy from hot charge carriers is an emerging research area with the potential to improve energy conversion technologies [1 2 3]. In chapter 2 of this thesis, I will present a novel plasmonic photoelectrode architecture carefully designed to drive photocatalytic reactions by efficient, non-radiative plasmon decay into hot carriers [4]. In contrast to past work, our architecture does not utilize a Schottky junction – the commonly used building block to collect hot carriers. Instead, large photocurrents were observed from a Schottky-free junction due to direct hot electron injection from plasmonic gold nanoparticles into the reactant species upon plasmon decay. Here, the key ingredients are (i) an architecture for increased light absorption inspired by optical impedance matching concepts [5] (ii) carrier separation by a selective transport layer and (iii) efficient hot-carrier generation and injection from small plasmonic Au nanoparticles with heterogeneous particle size distribution to adsorbed water molecules. The quantum efficiency of hot electron injection for different particle diameters were investigated in order to elucidate potential quantum effects while keeping the plasmon resonance frequency unchanged. Interestingly, our studies did not reveal differences in the hot-electron generation and injection efficiencies for the investigated particle dimensions and plasmon resonances.

In chapter 3, a simple strategy is presented to prepare free-standing through-hole ultrathin alumina membranes (UTAMs) for efficient sub-100 nm nanoarray fabrication that, in contrast to past works, can be generalized to any substrate and material [6]. Using developed strategy, a centimeter-scale of neat plasmonic photocathodes consisting dense array of sub-100 nm

plasmonic nanodots on top of very susceptible substrate of NiO_x thin film were fabricated. In addition, rough substrates of ~ 940 nm thick FTO (33 nm RMS, about 200 nm peak- peak surface roughness) and ~150 nm thick ITO (0.8 nm RMS, 7 nm peak-peak surface roughness) is successfully decorated with highly density of sub-100 nm nanodots array. To test the capability of developed route for efficient nanoarray fabrication on general substrate, a typical plasmonic photocathode was fabricated and employed for direct plasmon-driven photoelectrocatalysis. The obtained results revealed great potentials for establishing foundation of AAO-based generic nanoarray fabrication for novel applications.

Acknowledgements

I would like to express my gratitude to my advisor, Professor Isabell Thomann, for giving me the opportunity to work with her research group at Rice University, and provided the resources, guidance and encouragement for this path.

I would like to thank all the Thomann group members for their bright discussions, feedback, and helps on my work.

Special thanks to Professor Halas and Professor Nordlander for participating in my defense committee.

I would like to acknowledge who gave me insights along my academic trail, especially Professor M.Reza Hormozi Nezhad, and Professor Mehdi Jalali-Heravi for their substantial encouragements during my academic journey.

I would like to thank my parents for their great love and support during all these years of my academic and non-academic life.

Finally, I would like to thank my wife, Parisa Shadabipour. She was always there cheering me up and stood by me through the good times and bad.

Table of Contents

List of Figures

Chapter 1: Introduction to plasmonic photocatalysis

1.1.Introduction

Conventional photocatalytic systems are generally utilizes semiconductors to generate active excitons (electrons-holes pairs) to drive redox reactions. However, their practical applications are limited due to two major issues: (i) low photocatalytic activity, (ii) lack of efficient light absorption. Photocatalytic activity can be explained based on ability of photocatalyst to convert absorbed light into electrons-holes pairs those needs to migrate to the surface of photocatalyst for initiation of corresponding redox reactions. In order to efficiently extract the photogenerated carriers, the thickness of semiconductor photoactive layer should be comparable to the carrier diffusion length of semiconductor-the distance that carriers randomly travel before recombination. The carrier diffusion length is generally a small number (< 100 nm) for most of semiconductors, and hence decreasing the thickness or size of photocatalyst nanoparticles close to the carrier diffusion length can alleviate the issue of carrier recombination. However, absorption probability within photocatalyst decreases along with decreasing absorption depth. Another issue is that the band gap of many high-performance photocatalytic materials like TiO_2 and ZnO are located in the near ultraviolet (UV) region (wavelength<400 nm) and therefore they can only absorb small fraction of solar spectrum, while most of the photocatalysts that exhibit significant response to visible light, such as CdS and Fe_2O_3, suffers from low photocatalytic activity and short-term stability. In principle, the characteristics of an ideal photocatalyst can be listed as: long-term stability and robustness, high absorption across UV/Vis region; facile carrier generation and separation; high carrier diffusion length to facile transport of generated carriers to liquid/semiconductor junction; having proper valance band (VB) and conduction band (CB) potential with respect to thermodynamic redox potential of corresponding reaction; showing high

surface catalytic activity with low reaction barrier; being cost effective; being chemically compatible and environmental benign.

The need to use sunlight more efficiently has sparked increasing research interest in visible-light photocatalysis. In this regard, plasmonic photocatalysis has recently come into the focus that utilize noble metal nanoparticles (Ag, Au, Pt) to overcome barriers of conventional photocatalysis, and improve efficiencies of photocatalytic process either in presence of co-existing semiconductor photocatalyst [10] [11] [12] or through direct photocatalysis in absence of any semiconductors [13] [14]. Taking advantage of the localized surface plasmon resonance, plasmonic photocatalysis has attracted a lot of attention for high-performance photocatalysis.

1.2. Classification of plasmonic photocatalytic systems

In terms of co-existence of plasmonic nanostructure and semiconductor in system, plasmonic photocatalysis has been classified to two arbitrary categories that are called indirect and direct plasmonic photocatalysis. Indirect plasmonic photocatalysis employs a combination of plasmonic nanoparticles and semiconductor photocatalyst to drive the reaction, while direct plasmonic photocatalysis only relies on plasmonic metal nanoparticles. Figure 1.1 shows different plasmonic systems based on contact form. Each of these systems has its own interesting features for photocatalysis.

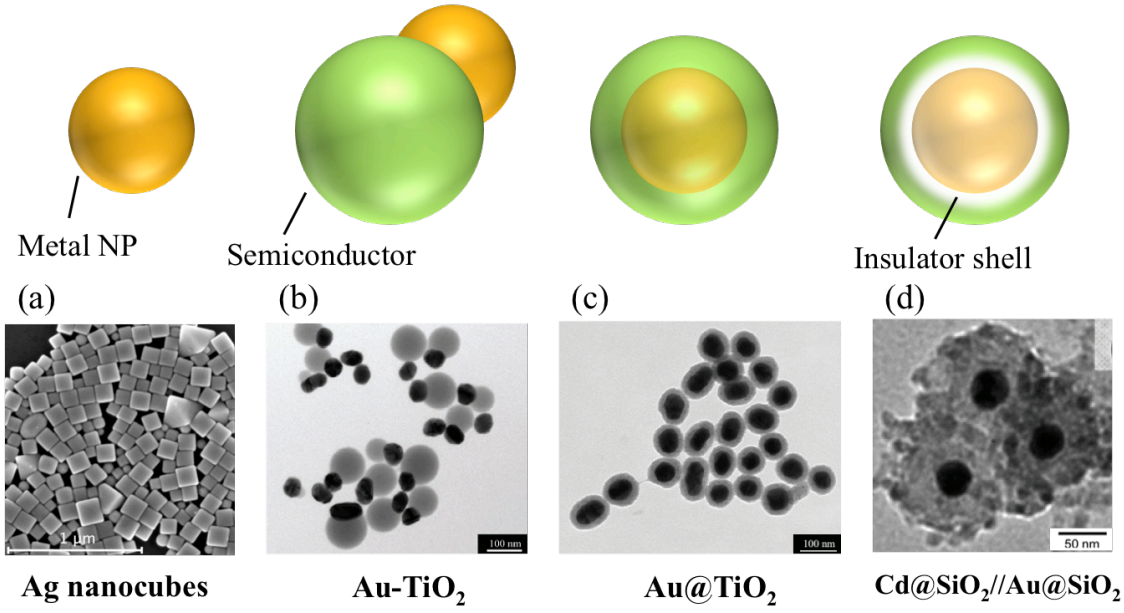

Figure 1. 1. Classification of the plasmonic photocatalytic systems based on the contact form. (a) Sole-metal form, used for direct plasmonic photocatalysis [15]. b-c indirect plasmonic photocatalysis, (b) Embedment form [16] (c) Encapsulation form [16] (d) Isolation form [12]. SC stands for semiconductor.

1.3. Enhancement mechanisms of plasmonic photocatalysis

Plasmonic nanostructures introduced several benefits to photocatalysis realms those are not accessible by conventional semiconductor photocatalysis [17] [18] [19]. Localized surface plasmon resonance (LSPR) and Schottky junction are two prominent features that benefit photocatalytic process through different mechanisms. Figure 1. 2. represents a schematic of plasmonic photocatalysis system of n-TiO_2/Au in embedment form. Schottky junction that results from the contact of the noble metal and the semiconductor leads to a builds up an internal electric field in the space-charge region at the interface of metal and semiconductor. The direction of electric field is toward the metal nanoparticles due to the nature of n-type semiconductor. Once the semiconductor is illuminated at the space-charge region or its proximity, internal electric field forces the photo-generated electrons and holes to move toward semiconductor and metals

nanoparticles, respectively [19]. As a result, charge separation increases and photogenerated carriers within semiconductor layer are more efficiently extracted. In addition, carrier diffusion length is reduced because the space-charge region is close to the surface and generated carriers travel a short way to reach the surface of photocatalyst. The metal nanoparticles also provide a fast lane for charge transfer (holes in the present case) and its surface acts as a catalytic site for photoreactions (oxidation reaction in this case).

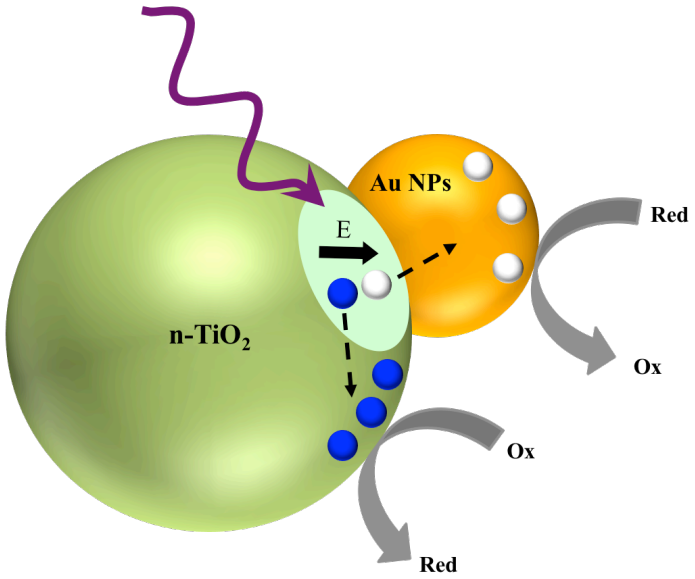

Figure 1.2. Schematic of plasmonic photocatalysis system of n-TiO_2/Au in embedment form. Schottky junction at metal/n-type semiconductor interface builds up an internal electric field in the space-charge region with its direction toward the metal nanoparticles. Once the semiconductor is illuminated at the space-charge region or its proximity, internal electric field forces the photo-generated electrons and holes to move toward semiconductor and metals nanoparticles, respectively.

The more prominent feature of plasmonic photocatalysis is the Localized surface plasmon resonance (LSPR) that has potential to bring several significant benefits to the photocatalysis. Some of the major benefits that have been verified so far are visible light response and enhanced UV/Vis absorption, enhancing local electric field, generating more

electron-hole pair powered by LSPR, local heating effect, reducing minority carrier diffusion length, enhanced interaction with molecules etc [19]. the optical properties and plasmon resonance wavelength of the silver and gold nanoparticles can be tailored thorough visible region and near-UV by changing the size, shape and refractive index surrounding environment. This boosts the UV/vis light response and raises the exciton generation rate. It should be noted that depending on the system, some or all of these effects may be presented, and also some features could have adverse effect on overall photocatalytic efficiency. Here three primary mechanisms is discussed that have been proposed for observed improvement of photocatalytic efficiencies of LSPR-assisted photocatalysis.

1.3.1. *Elastic light scattering by plasmonic particles*

Elastic scattering of resonant photons by the plasmonic structure increases the average photon path passes through the system, and therefore more light is being absorbed by active absorber layer that is expected to increase the concentration of photogenerated carriers (Fig. 1.3). The scattering mechanism is larger for nanoparticles with size typically larger than 60nm for that the Mie scattering has major contribution to the extinction compare to the absorption. In this condition, the surface of the particles essentially acts as a nanomirror and can scatter some resonant photons that are not absorbed by the semiconductor on first pass through, increasing the average photon path length, and consequently produce more absorption near the semiconductor surface.

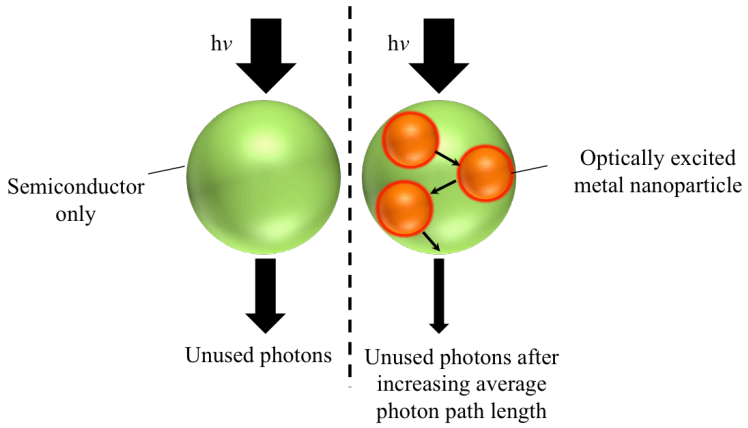

Figure 1.3. Schematic illustrating the scattering mechanism by the plasmonic nanoparticles surface that leads to an enhancement of the optical absorption through increasing the average path length of photons in the composite structure.

1.3.2. *Plasmonic near-field energy transfer*

So far, plasmonc Local electromagnetic field enhancement (LEMF) and near-field energy transfer has been presented to have major contribution for enhancing photocatalytic efficiencies in plasmonic photocatalyst systems [3 15 16 20 21 22 23 24]. Local electric field enhancement is an immediate effect of localized surface Plasmon resonance and interaction of semiconductor with the LSPR-induced electric fields at the metallic nanostructure results in permeating strong electric field into the neighboring semiconductor that allows for selective formation of carriers in the near surface region of semiconductor (Figure 1.4.). It is clear that the most efficient carrier generation happens when the LSPR frequency of plasmonic nanostructure highly overlaps with absorption maxima of semiconductor. The photogenerated carriers are readily separated and are available for performing photocatalytic redox reactions as they are close to semiconductor surface and therefore carrier recombination is less likely. The enhancement factor ($(E/E_0)^2$) is proportional to the ratio of the local electric field amplitude |E| to the original electric field $|E_0|$. This mechanism is often where plasmonic nanostructure and semiconductor are separated by the

dielectric layer, which prevents direct contact and carrier exchange between metal and semiconductor. Intensity of the electric field is spatially non-homogenous with highest intensity at the nanoparticles surface and exponential decay by increasing the distance from surface of the nanoparticle. Therefore, there is strong electric field at the interface of the metal nanostructure and semiconductor that boosts optical transition and consequently rate of carrier generation within semiconductor by a roughly linear relationship [19].

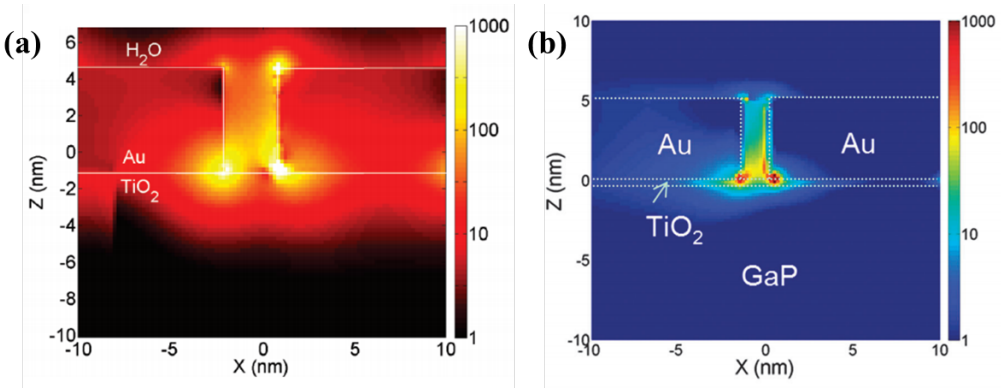

Figure 1.4. Typical optical simulations of different structure showing SPR-enhanced electric fields owing to photo-excited Au particles, permeating into a underlying TiO_2 substrate [21] (a) and nominal TiO_2 spacer layer between Au and GaP substrate [24] (b). The color bar shows electric field intensity normalized by the light source intensity ($|E|^2/|E|_0^2$).

1.3.3. *Non-radiative plasmon decay into hot carriers*

The term hot-electrons refers to the electrons generated as a result of illuminating materials with highly energetic photons with energies exceed the work function of the material. These incoming photons usually have wavelength in the UV region, and the hot electrons with energies higher than work function of the material can be emitted results in producing photocurrent. As the most part of the solar spectrum fall into the visible and near-IR regions with less energetic photons that causes practical application of this effect to be impossible. However,

the recent discovery in the field of plasmonic revealed that the hot-electrons can be generated in the plasmonic structures utilizing photons with energies in visible region [1 2 25 26]. After LSPR-excitation in plasmonic structures, plasmon decay takes place in femtosecond time scale releasing its accumulated energy either in radiative or non-radiative form. The radiative palsmon decay results in near-field enhancement. Non-radiative Plasmon decay, however, involves in energy transfer to the electrons through intraband excitations or through interband excitations resulting from transitions between other bands (for example, d bands) and the conduction band. This generates highly energetic hot-electrons that can be extracted to produce photocurrent or drive photocatalytic process.

The generated hot-electrons have very short life time due to electron-phonon interactions [27], and other fast relaxation processes. Hence, hot carriers need to be harvested on femtosecond to picosecond timescales. Employing Schottky barrier has been well-adopted approach for harnessing hot carriers in plasmon-based device for different applications [28 29 30 31 32 33 34 35]. This approach involves charge (hot-electron) injection from metal nanostructure to the conduction band of neighboring n-type semiconductor. If the size of the nanoparticles is big enough for that size-dependent bandgaps is negligible (the metal nanoparticles has continuous band structure and follow the Fermi–Dirac distribution), hot electron injection involves three steps, as is shown in figure 1.5. For n-type semiconductor with direct electrical contract with the metal nanoparticles, upon illumination of nanoparticles at the SPR wavelength, the generated hot-electron with energy higher than Schottky barrier feed into the CB of the neighboring semiconductor (Fig. 1.5a). As a result, the energy states of electrons are changed back to the Fermi–Dirac distribution, but at a higher Fermi level ($E'_f > E_f$) (fig. 5b). Electron with energy >Ef continues

feeding into the conduction band and after complete decay of surface plasmon energy, the electrons in the metal nanoparticle return to the standard Fermi–Dirac distribution (fig. 1. 5c).

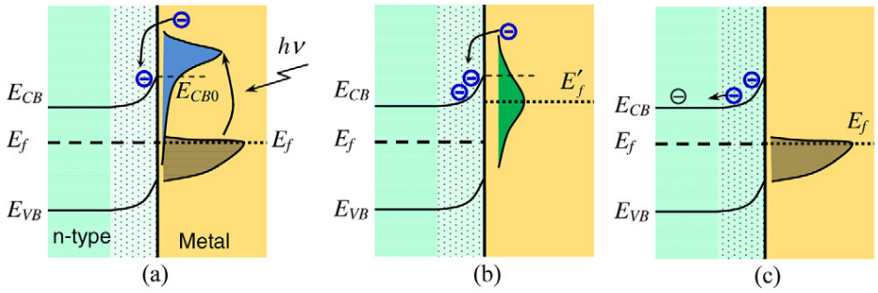

Figure 1.5. LSPR sensitization effect results in direct electron transfer from metal nanoparticles to the n-type semiconductor [19].

Figure 1.6 represents a schematic of plasmon-induced hot-electron injection over Schottky barrier of the neighboring semiconductor to drive water splitting reaction.

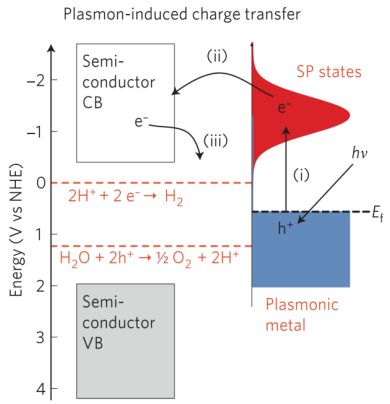

Figure 1.6. Mechanism of SPR-induced charge transfer with approximate energy levels on the NHE scale. Dashed red lines refer to the water-splitting redox potentials. (i) Electrons near the metal Fermi level, E_f are excited to surface plasmon (SP) states; (ii) the electrons transfer to a nearby semiconductor particle; (iii) this activates electron-driven processes such as the hydrogen-evolution half-reaction [3].

In chapter 2, I present detailed look at our recent findings on direct plasmon-driven photoelectrocatalysis of water through efficient hot-electron generation and direct injection from a novel architecture that avoid a Schottky interface for harvesting hot-electrons [4].

In chapter 3, I describe a simple developed strategy for preparing free-standing through-hole UTAMs for efficient sub-100 nm nanoarray fabrication that can be generalized to any substrate and material [6]. In this regard, a typical fabricated plasmonic photocathode consisting sub-50 nm Au nanoarray is successfully applied for direct plasmon-enhanced photoelectrocatalysis of water.

Finally, chapter 4 incudes device fabrication and methods used to conduct experiments and measurements to obtain the results in chapter 2 and 3. This chapter also explains the theoretical method to support the experiment.

Chapter 2: Direct plasmon-driven photoelectrocatalysis [4]

2.1. Introduction

Plasmonic metal nanostructures are currently receiving considerable attention in the quest for efficient solar-to-fuel energy conversion, in large part owing to their unique light harnessing capabilities associated with their localized surface plasmon resonance (LSPR) features [3 17 18 20 21 28 32 36 37 38 39 40 41]. LSPR-assisted solar-to-fuel energy conversion [3 19 42] has been shown to utilize three primary mechanisms, (I) elastic light scattering by plasmonic particles, (II) plasmonic near-field energy transfer [20], and (III) non-radiative plasmon decay into hot carriers [32 43 44 45 46 47 48 49]. In particular this last mechanism is emerging as a hot topic, since the utilization of hot carriers to drive chemical reactions may open up pathways that are inaccessible by conventional methods such as heating or applying an electrochemical bias [2 26]. Past demonstrations of hot-carrier utilization focused on employing a Schottky barrier for hot-electron extraction. In this scenario, only hot-electrons with sufficient energy to overcome the Schottky barrier can be collected from the conduction band of the semiconductor [28 32 40 29] and spatially separated from the holes left behind in the metal nanostructure. Such Schottky barriers have been the central building block for harnessing hot carriers in plasmon-based photodetectors [50 51], sensors [52], photovoltaic and photocatalytic devices [2 26 53 54 55].

Herein, an alternative architecture is described to achieve efficient and direct injection of hot electrons from plasmonic gold nanoparticles to adsorbed water molecules for solar water splitting in a Schottky junction-free device. Fig. 2.1 shows our plasmonic photoelectrode structure. Here, a selective transport layer facilitates carrier separation. The resulting enforced confinement of electrons within the nanoparticles opens up a new pathway for direct injection of hot electrons into the unoccupied orbitals of adsorbed water molecules. The present architecture

is also designed to maximize light absorption within the layer of small gold nanoparticles. It is inspired by optical impedance matching concepts [5 56], where the optical function of NiO_x is to serve as a wide bandgap spacer layer between the plasmonic nanoparticles and the aluminum back reflector. The spacer layer thickness can be adjusted to achieve maximum absorption within the gold nanoparticles based on electromagnetic simulations. Two samples consisting of Au hemispheres with distinct dimensions: (i) 30 nm diameter, 6 nm thick, and (ii) 10 nm diameter, 2 nm thick were investigated. Henceforth those will be referred as 30 nm and 10 nm diameter particles, respectively.

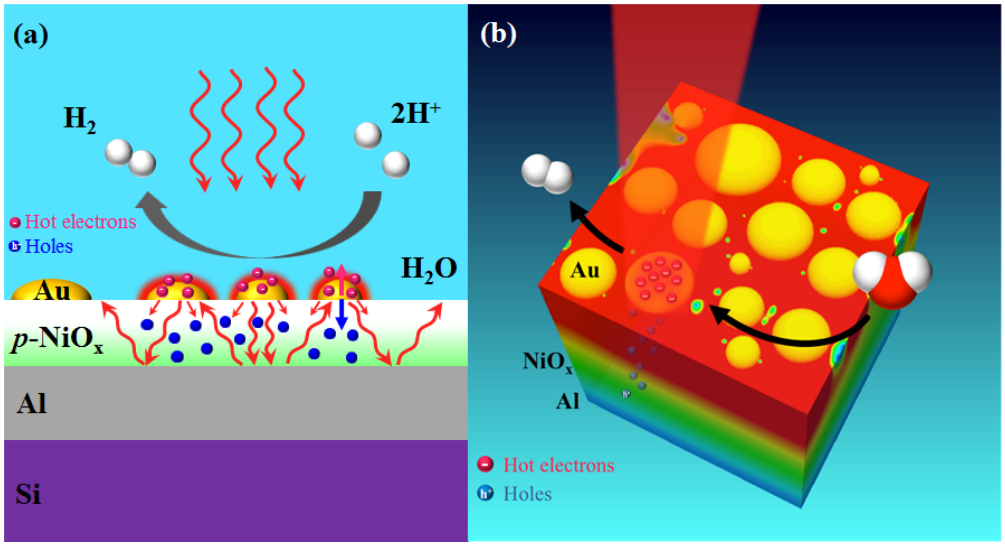

Figure 2.1. Structure and mechanism of operation of our plasmonic photocathode for plasmon mediated direct electron injection to drive solar-to-chemical energy conversion. a) Schematic of plasmonic photocathode for solar water splitting, consisting of Au nanoparticles with heterogeneous particle size distribution in direct contact with water, p-NiO_x as an electron blocking layer and aluminum as the electrode material. b) Simulated field distribution withing photocathode architecture consisting heterogeneous particle size distribution (average 10 nm, 2 nm thick) upon illumination and phenomena happening therein.

The utilization of hot electrons has generally been hampered by their extremely short relaxation lifetimes due to electron-phonon interactions [27] and other fast relaxation processes. Hence, hot carriers need to be harvested on femtosecond to picosecond timescales. Recent work in the area of solar water splitting [21] and photocatalytic CO_2 reduction [22] has begun to investigate the efficiency and the lifetime of hot-electrons generated via plasmon decay at semiconductor/metal Schottky interfaces. Kim et al. [39] studied Au particles larger than 50 nm and observed that the quality factor of the plasmon resonance is directly related to the photocatalytic activity of the particles. Qian et. al. [57] found that small plasmonic Au particles cannot inject a sufficient number of hot electrons into the conduction band of TiO_2 to raise the energy level sufficiently to drive the hydrogen evolution reaction (HER). DuChene et. al. [45] found an increased lifetime of excited-state carriers in plasmonic Au/ TiO_2 heterostructures compared to bare TiO_2. And recently, plasmon-induced hot carrier generation has culminated in a report demonstrating an autonomous device for solar water splitting based on a plasmonic gold nanorod array/TiO_2 Schottky junction [32]. Unfortunately, the injection efficiency of hot carriers at a Schottky interface is extremely low, in large part owing to the momentum mismatch of hot electrons traversing the junctions [58]. Therefore, novel architectures that avoid a Schottky interface can potentially improve the efficiency of hot electron devices. The efficiency could be further increased if momentum conservation can be relaxed, e.g. by hot electron injection from small-sized plasmonic particles into molecules. Smaller metal nanoparticles are also advantageous since they facilitate the efficient decay of plasmons into energetic hot carriers [27]. From an optical perspective small plasmonic particles, however, have a smaller absorption cross section than larger particles making it challenging to achieve complete light absorption, and correspondingly efficient hot carrier generation, within these particles. From an electrical

standpoint charge recombination must be avoided by fast separation of oppositely charged carriers. The present device is a novel plasmonic photoelectrode architecture that achieves a combination of high optical absorption within small Au NPs, efficient charge separation by a hole-transporting but electron-blocking layer, and efficient hot carrier injection into adsorbed water molecules.

2.2. Results and Discussions

Figure 2.2 shows the energy schematic of our structure. Here, sun light resonantly excites plasmons in gold nanoparticles, which subsequently decay into hot electrons. The hot electrons are directly injected into water molecules to drive the hydrogen evolution reaction. The electronic function of the NiO_x layer [59] is to block electron transport while allowing for hole transport to the aluminum back electrode and further through the external circuit to the platinum counter electrode.

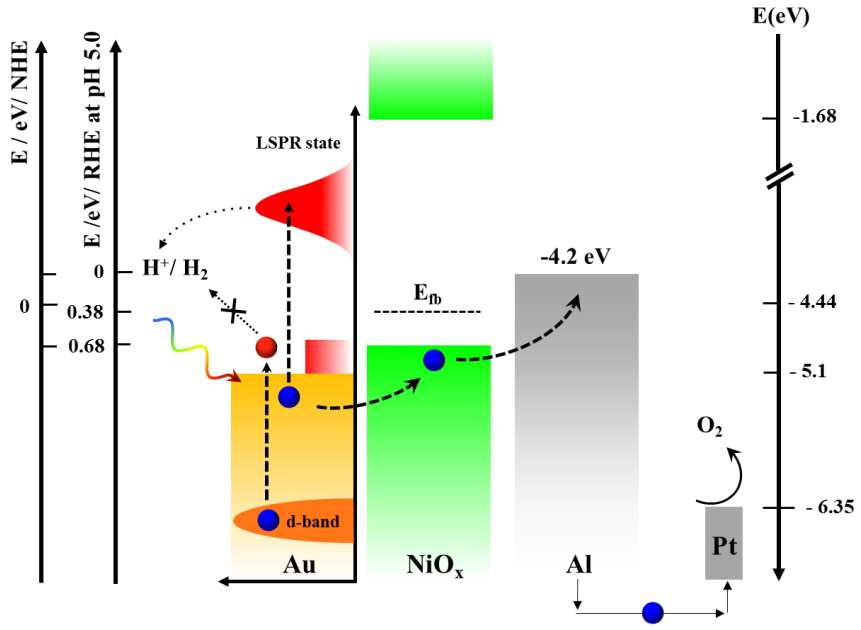

Figure 2.2. Energy schematic and mechanism of operation of our plasmonic photocathode for plasmon mediated direct electron injection to drive the hydrogen evolution reaction. Small metal nanoparticles facilitate the efficient decay of plasmons into hot carriers. Here the hot electron is directly

injected into water molecules to drive the hydrogen evolution reaction. A NiO_x layer blocks electron transport while allowing hole transport to the platinum anode. Note that this novel plasmon-induced hot carrier generation mechanism for water splitting does not rely on a semiconductor/metal Schottky junction to collect hot-electrons.

Figure 2.3 Shows SEM images of the Au nanoparticles formed from annealing different thicknesses (2 nm, 6 nm, 10 nm) of Au films on NiO_x and the insets show the corresponding particle size distributions. We found that evaporation of a nominal thickness of 2 nm Au on top of a 40 nm thick NiO_x film and subsequent annealing results in the formation of well-separated particles with a diameter of 10 nm and a narrow particle size distribution (Fig. 2. 3a). For 6 nm thick Au, particle diameters around 30 nm with a broader particle size distribution (Fig. 2. 3b) were obtained. However this distribution does not contain the smallest particle diameters (i.e. 2 to 5 nm diameter Au NPs) that are only present in the 2 nm thick evaporated Au films. When the evaporation thickness is increased to 10 nm, large gold nanoislands with typical sizes larger than 150 nm were formed after annealing of the sample (Fig. 2.3c).

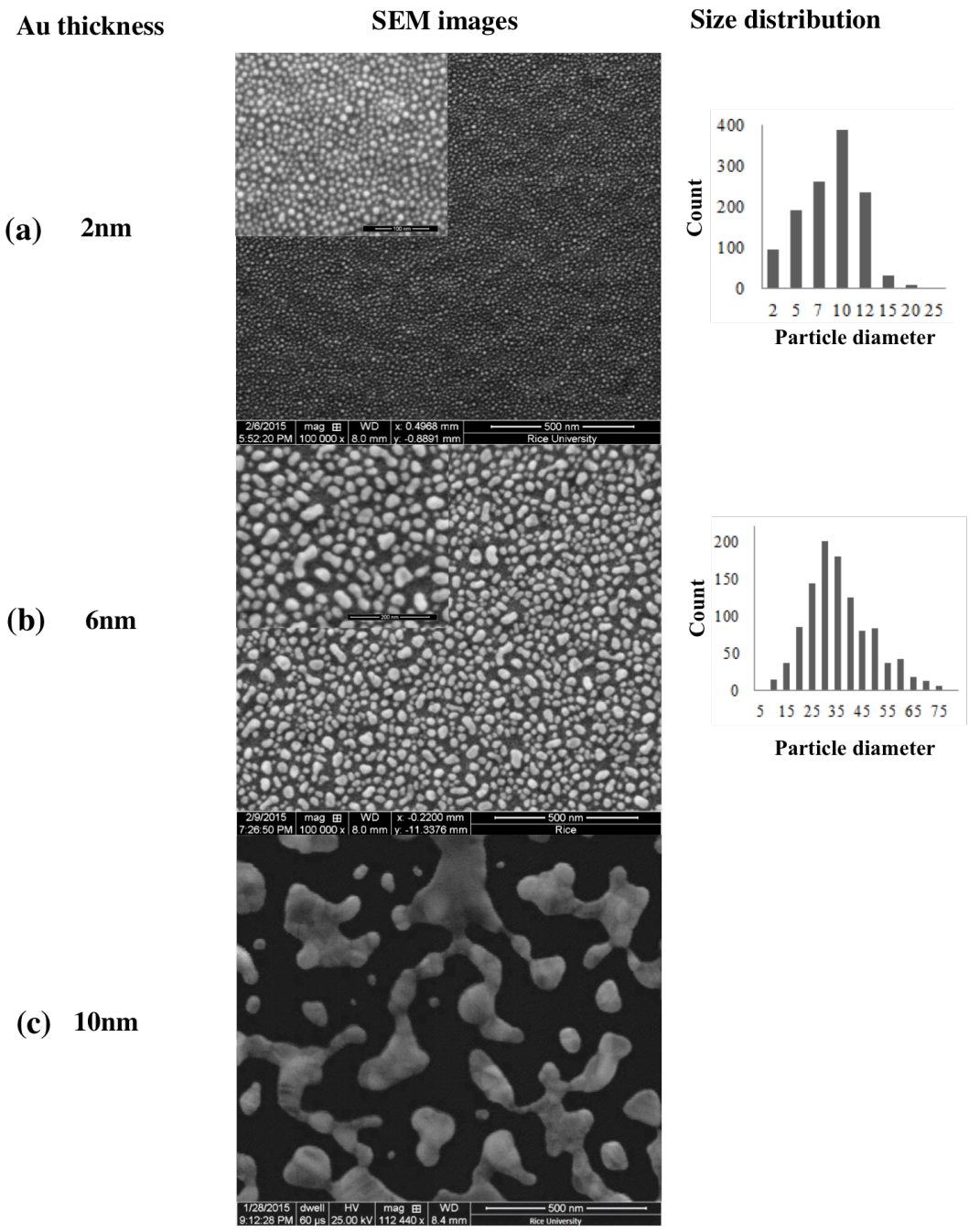

Figure 2.3. SEM images and corresponding particle diameter distributions for particles formed from the deposition of a 2nm (a), 6nm (b), and 10 nm (c) thick Au film on 40 nm thick NiO_x spacer layer.

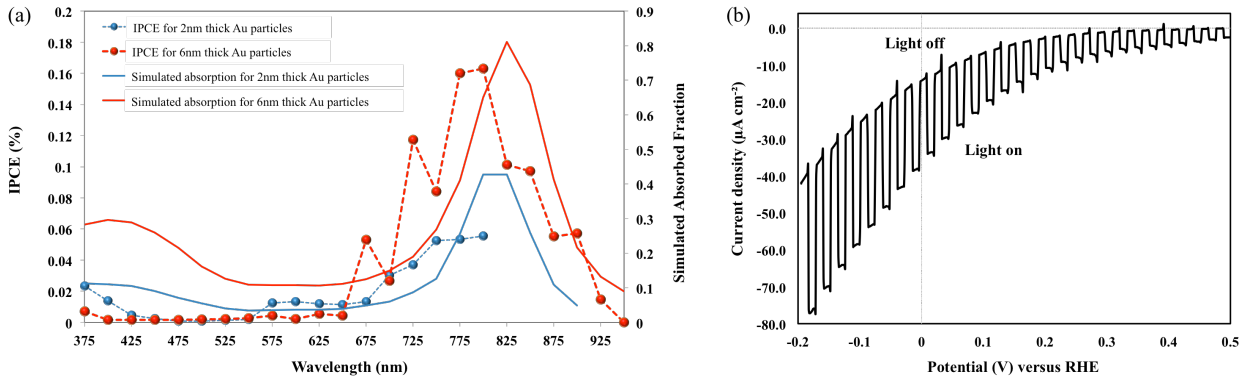

Figure 2.4. Photocatalytic performance of our structures. a) Comparison between measured IPCE (left axis) and simulated absorbed fraction (right axis) versus wavelength in 2nm (blue) and 6 nm (red) thick gold nanoparticles. Note, electromagnetic simulations of the absorbed fraction were performed for gold nanoparticles with 10 nm (2nm thick) and 30 nm diameter (6 nm thick), respectively. The spectral dependence of simulated and experimental data shows convincingly that the photocurrent originates from plasmon-induced hot carriers within the gold nanoparticles. b) Photocurrent generated from a plasmonic photocathode decorated with 2 nm thick particles in nitrogen-purged, 0.5M Na_2SO_4 electrolyte buffered at pH 5.2. The total white light illumination intensity was 100 mW cm^{-2}. The photocurrent was measured in a three-electrode photoelectrochemical cell configuration with a Pt mesh as the counter electrode, and is plotted versus the reference hydrogen electrode (RHE). The scan rate was 2 mV/s.

To investigate the mechanism of plasmon mediated photocatalysis in the present Schottky junction-free plasmonic photocathode, wavelength-resolved photocurrent measurements were performed in a range from 375 nm to 950 nm. These measurements were performed in a three-electrode photoelectrochemical cell in a nitrogen-purged solution of 0.5 M Na_2SO_4 buffered at pH 5.2. The photocathode consisted of NiO_x/Al samples decorated with polydisperse Au nanoparticle size distributions (with diameters of most frequent occurrence) centered around 10 nm and 30 nm, respectively (see experimental and methods for detailed fabrication process). A proper insight into the possibility of direct hot-electron generation and injection into water after

non-radiative plasmon decay can be gained by comparing the wavelength-resolved incident-photon-to-current conversion efficiency (IPCE) with numerically simulated absorption spectra. This comparison is provided in Fig. 2.4a. For both samples (10 nm and 30 nm diameter Au NPs) the measured IPCE maxima match with the simulated absorbed fraction within the gold NPs. The measured IPCE for 30 nm Au NPs is approximately three times as large as that of the 10 nm Au NPs. We performed electromagnetic simulations of light absorption within the gold nanoparticles using the finite difference time domain (FDTD) method. For our electromagnetic simulations we chose the most frequently occurring particle diameters in our samples (30 nm and 10 nm, respectively) based on the experimentally determined particle size distribution in our scanning electron microscope (SEM) images shown in Fig. 2.3. Both numerical structures employ gold nanoparticles with an anisotropic shape with a 5:1 diameter-to-thickness aspect ratio (30 nm: 6 nm and 10 nm: 2 nm, respectively). The anisotropic shape is the reason for the plasmon resonance being shifted to the near-infrared around 800 nm. Finite difference time domain (FDTD) simulations was performed to maximize light absorption within the 30 nm diameter, 6 nm thick gold nanoparticles by optimizing the NiO_x spacer layer thickness.

The numerical absorbed fraction reaches about 80% for the 30 nm particles and about 50% for the 10 nm particles for the same NiO_x spacer layer thickness of 40 nm (Figure 2.5.). The absorbed fraction in the 10 nm Au NPs could be similar high as for the 30 nm Au NPs by employing an 80 nm thick NiO_x spacer layer (Fig. 2.5a) but here we decided to keep the NiO_x film thickness the same in order to keep the electronic properties for both samples the same. As expected, the simulated absorbed fraction within the Au NPs shows increased absorption for both samples at wavelengths below 525 nm due to interband transitions from the occupied d-band. However, the absorption due to interband transitions does not result in a measurable cathodic

photocurrent in the 450 nm to 550 nm wavelength region. The reason is that electrons excited from the d-band are promoted to unoccupied states near the Fermi level, and therefore are not energetic enough to drive the hydrogen evolution reaction (see Figure 2.2.). We observe a small photocurrent below 425 nm close to the band gap of $NiO_{x,}$ which can be attributed to light absorption in the NiO_x.

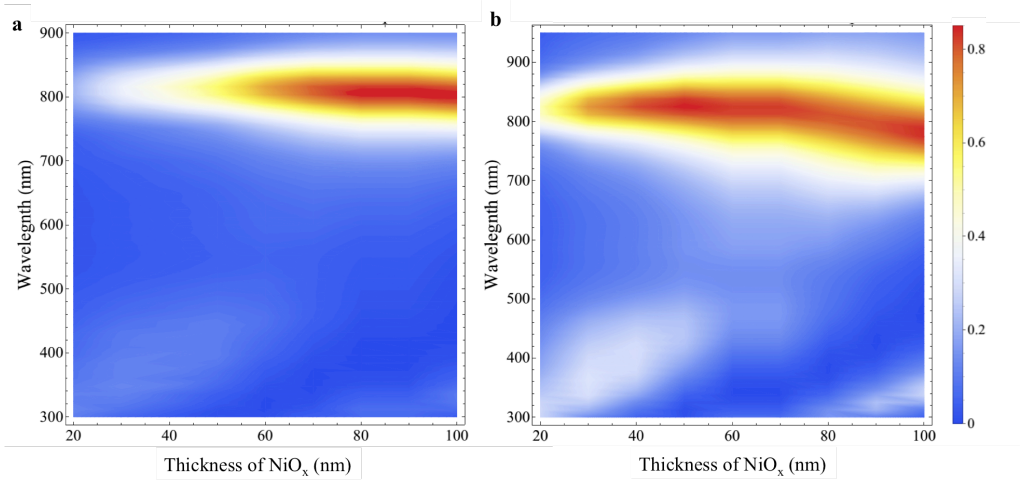

Figure 2.5. The simulated absorbed fraction of light within the Au NPs for a) 2 nm and b) 6 nm thick Au NPs versus thickness of NiO_x. Both numerical structures have gold nanoparticles with an anisotropic shape, but the 5:1 diameter-to-thickness aspect ratio is maintained (30 nm: 6 nm and 10 nm: 2 nm, respectively).

We performed control experiments to establish that the measured photocurrent arose from a direct electron transfer from Au NPs to protons in water, rather than from any enhancement in the NiO_x. Cyclic voltammetry measurements were carried out in structures with and without Au nanoparticles. At an electrode potential of 0V vs. RHE, we observed photocurrents of 25 $\mu A/cm^2$ with Au NPs (Fig. 2. 4b) and 0.250 $\mu A/cm^2$ without Au NPs (Fig. 2.6a), respectively. Thus, the photocurrents without Au NPs are ~100x smaller than with Au NPs. We also conducted wavelength-resolved photocurrent measurements of our NiO_x/Al samples without Au NP in the wavelength range from 375 nm to 900 nm at an electrode potential of -0.1 vs. the RHE. No

photocurrent was observed from 500 nm to 900 nm demonstrating that the photocurrent observed in the Au-containing structure does not originate from defect or trap states in the NiO_x. However, a photocurrent of approximately - 0.25 $\mu A/cm^2$ is found at 375 nm, which is near the bandgap of NiO_x (Fig. 2. 6b).

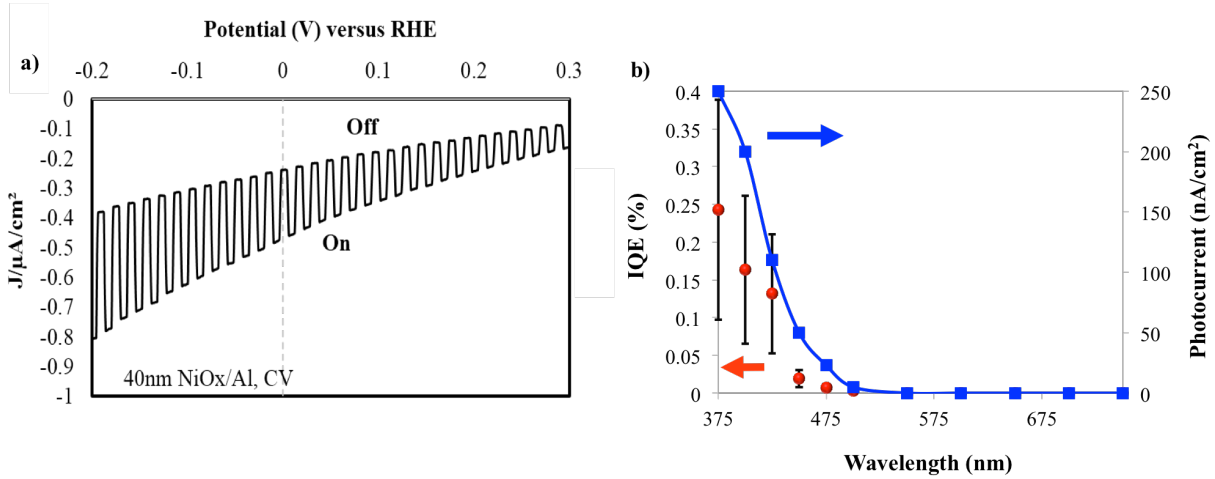

Figure 2.6. Control experiment for NiO_x/Al structure without Au nanoparticles. a) Current versus potential behavior of NiO_x/Al under chopped illumination at one sun (100 mW/cm^2) immersed in a nitrogen-purged solution of 0.5 M Na_2SO_4 buffered at pH 5.2. A three-electrode photoelectrochemical cell was used with a Ag/AgCl (in sat. 3.0 M KCl) and a Pt mesh as the reference and the counter electrode, respectively. The photocurrent is approximately 0.08 $\mu A/cm^2$ at an electrode potential of 0.3 V vs. RHE and reaches 0.250 $\mu A/cm^2$ at 0V vs. RHE. The scan rate was 2 mV/s. b) Calculated internal quantum efficiency (IQE) and measured wavelength-resolved photocurrent for a NiO_x/Al control experiment. The symbols show the internal quantum efficiency (left axis), and the solid line (right axis) shows the measured photocurrent. Photocurrent measurements were taken at a low cathodic overpotential of -0.1 V versus the RHE and at a pH of 5.2.

We also performed Mott Schottky measurements of our 40 nm thick NiO_x film (Appendix E), and found that the material is intrinsically p-type with a hole concentration of 10^{18}-10^{19} cm^{-3} and its flat band potential lies very close to the Fermi level of gold. This means, the Fermi level of

the gold nanoparticles is very close to the valence band of NiO_x and thus no charge transfer to a trap state near the conduction band (which is almost 3.5 eV away (see Appendix E) can be driven by a plasmon resonance of 800 nm (≈ 1.55 eV).

Given that these control experiments did not produce appreciable photocurrents, we propose the following mechanism for the observed IPCE of 0.1 %: Light absorption is enhanced by exciting localized surface plasmon resonances in a gold nanoparticle/spacer/reflector geometry. Plasmon quanta decay into electron-hole pairs. The plasmon resonance frequency of our photocathode lies at around 800 nm – 825 nm, thus we expect a maximum energy of ~1.55 eV for hot-electrons generated from the surface plasmon resonance. The electrons possess a non-equilibrium Fermi-Dirac distribution where the tail of the distribution has enough energy to overcome the energy barrier required for driving the hydrogen evolution reaction with a redox potential that lies at excitation energy of about 1 eV above the Fermi energy of the Au NP. In other words, hot electrons with energies greater than 1 eV plus the required overpotential should be able to transfer directly into the unoccupied states of the reactant species and thus result in the initiation of the photocatalytic HER. The favorable band edges of p-NiO_x allow for hole transfer while blocking electron injection. The holes collected by NiO_x are then collected by underlying aluminum and transported to the counter electrode to balance the reaction. Although the nature of carrier transport in NiO_x has not been fully unraveled, a growing consensus supports the small polaron hopping mechanism [60].

Figure 2. 4b shows the current versus potential of a plasmonic photocathode decorated with 10 nm diameter nanoparticles under chopped illumination at one sun (100 mW/cm^2) immersed in a nitrogen-purged solution of 0.5 M Na_2SO_4 buffered at pH 5.2. A three-electrode photoelectrochemical cell was used with Ag/AgCl (in sat. 3.0 M KCl) and a Pt mesh as the

reference and the counter electrode, respectively. The photocurrent is approximately 2.6 μA/cm^2 at 0.5 V vs RHE and reaches 24 μA/cm^2 at zero versus the RHE. We also performed chronoamperometry measurements at -0.1 V vs. RHE and observed a photocurrent of 26 μA/cm^2 for 30 nm diameter Au NPs and of 13 μA/cm^2 for 10 nm diameter Au NPs at a light intensity of 100 mW cm^{-2} (Figure 2.7.). These observed photocurrents are on a par with a recently demonstrated large catalytic surface area TiO_2-coated plasmonic gold nanorod array Schottky junction geometry that in addition added platinum nanoparticles to catalyze the HER reaction [32].

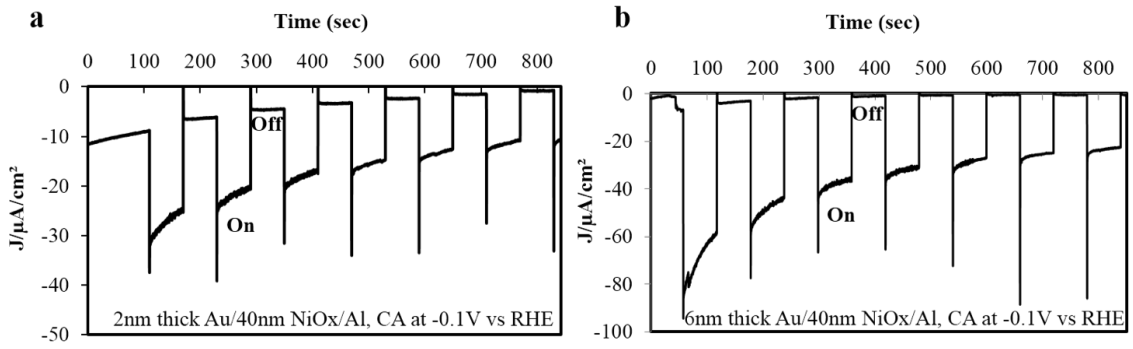

Figure 2.7. Photocurrent density response of plasmonic photocathode decorated with 2 nm thick (10 nm particle size) (a) and 6 nm thick (30 nm particle size) Au NPs (b), under chopped illumination (at a light intensity of 100 mW cm^{-2}) and at a low cathodic overpotential of -0.1 V versus the RHE. Nitrogen-purged 0.5 M Na_2SO_4 buffered at pH 5.2 was used as the electrolyte solution. Ag/AgCl (in saturated 3.0 M KCl) and a Pt mesh were used as a reference and counter electrode, respectively.

The absorption spectrum of a plasmonic device is generally influenced by the size, shape, environment and distribution of the plasmonic particles and thus these are important parameters for tuning plasmon-mediated catalysis. These parameters do not only affect the wavelength of the plasmon resonance but also the efficiency of hot carrier generation and injection [2, 27, 61]. In Figure 2.8., a comparison of the internal quantum efficiency (IQE) for 10 nm diameter and 30 nm diameter Au particles is presented. The solid curve shows the internal quantum efficiency

(left axis), and the symbols (right axis) show the measured photocurrent. The IQE was calculated from the measured photocurrent and the measured absorbed fraction (Fig. 2.9.).

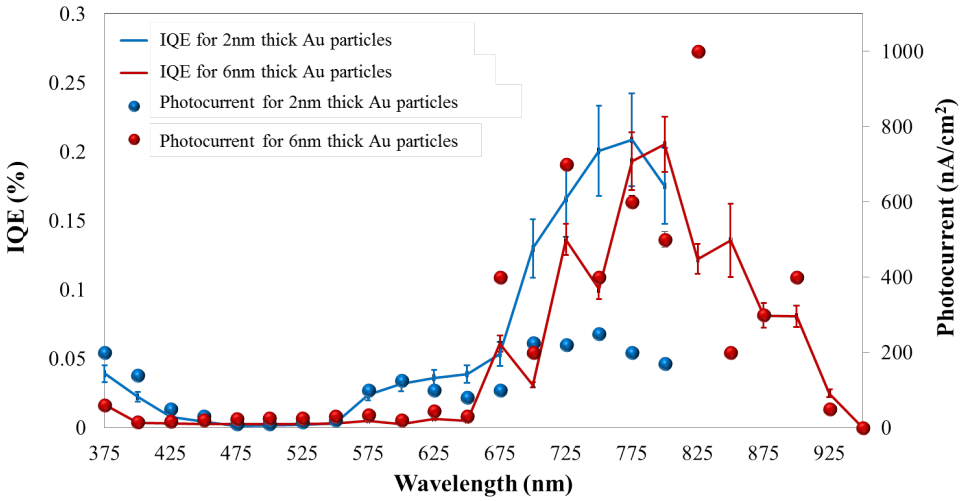

Figure 2.8. Comparison of the internal quantum efficiency (IQE) for small (10 nm diameter, 2 nm thick) and large (30 nm diameter, 6 nm thick) Au particles with the same plasmon resonance wavelength. The solid curve shows the internal quantum efficiency (left axis), and the symbols (right axis) show the measured photocurrent. We find that the IQE is comparable for small and large particles, suggesting that hot electron generation and injection efficiencies are similar and quantum size effects (i.e. wavefunction spill out) are not important for our 10 nm diameter gold particles.

The IQE for 10 nm and 30 nm diameter particles is the same, demonstrating that both size particles are equally efficient in terms of hot electron generation and injection. The observation of an identical IQE for these two different particle sizes is surprising in light of recent results from Manjavacas et al [27]. These authors studied the hot electron generation efficiency as a function of the carrier lifetime and the particle size. A general feature of such a mechanism is that longer lifetimes result in the generation of hot carriers with large energies while larger diameters produce less energetic electrons at a fixed lifetime. Since the energy distribution of the

hot electrons can dramatically change by simply varying any or both of these parameters, the diameter of the Au NP should have a significant influence on the internal quantum efficiency. Manjavacas et al. have theoretically found that for 10 nm diameter spherical silver nanoparticles plasmons decay into the most energetic hot carriers. Here, we conclude that in our experimental work, in which we investigated a different particle shape, material and environment compared to the work of Manjavacas et al., quantum effects do not play a significant role when decreasing the diameter of our asymmetrically shaped gold nanoparticle distributions from 30 nm to 10 nm. The IQE reaches about 0.2 %, and the hot electron generation and injection efficiency are the same at longer wavelengths from 675 nm to 900 nm for our particle distributions centered around 10 nm and 30 nm, respectively.

Interestingly, we observe a small photocurrent and an IQE of 0.02% in the 575 nm to 650 nm wavelength region for the 2 nm thick Au NPs but not for the 6 nm thick Au NPs. We attribute the photocurrent and the IQE in this wavelength region to the 2 nm to 5 nm diameter particles that are only present in our 2 nm thick Au NP samples, but not in the 6 nm thick Au NP samples. The measured IQE in this wavelength region is ten times lower than in the region above 650 nm, and the particle size distribution from the SEM image suggests that about one third of the particles have diameters smaller than 5 nm. Therefore, our data suggest that the IQE on a per-particle basis, i.e. the hot electron generation and injection efficiency per particle, is not enhanced for 2 to 5 nm diameter particles. For samples decorated with larger Au islands from 10 nm thick evaporated Au films, we observed only a small photocurrent less than 0.5 $\mu A/cm^2$. These observations are consistent with predictions that larger size particles do generate less energetic hot carriers [27].

We employed a heterogeneous particle size distribution on top of our spacer/reflector electrode to achieve broadband light absorption, in contrast to the simulated monodisperse 30 nm diameter Au particles which only support light absorption in a relatively narrow region with a FWHM of 100 nm centered around 830 nm. The numerically calculated absorbed fraction for a periodic array of monodisperse 30 nm diameter gold nanoparticles can reach approximately 80 % within the Au NPs and 95 % in the total structure around 830 nm (FWHM of 100 nm) (see Figure 2. 9a). The absorbed fraction could be further enhanced by e.g. coating the Au NPs by another dielectric material that better fulfills the critical coupling condition [5]. Experimentally we fabricated a heterogeneous particle size distribution with Au NP diameters of most frequent occurrence around 30 nm by annealing 6 nm thick Au films on top of NiO_x. Measurements from SEM images show that the distribution of particle diameters varies from 10 nm to 80 nm. As expected from the broad particle size distribution, we observe a substantial spread in particle plasmon resonances leading to a substantial broadening of the experimentally measured absorbed fraction curve. In Figure 4a we show the measured total absorbed fraction in air of photocathodes with 6 nm thick Au NPs. These samples appear blue in color. As can be seen from the measured absorption data, the photoelectrode is an efficient light absorber at wavelengths above ~ 500 nm. We also show the simulated total absorbed fraction for a photocathode in water employing a periodic array of 30 nm, 20 nm, 10 nm diameter gold particles with a separation of 15 nm, 10 nm, 5 nm, respectively. Our simulations qualitatively support the notion that broadband absorption is possible in these structures. The simulations also show that there is no plasmon resonance peak below 600 nm, in agreement with the experimentally observed low photocurrent in that wavelength range.

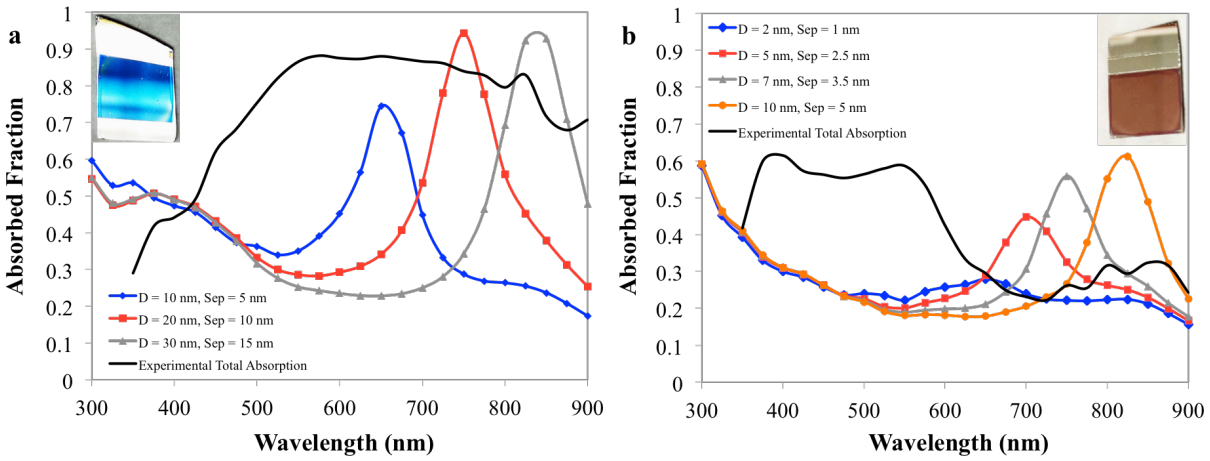

Figure 2.9. Experimentally measured total absorbed fraction for photocathode with 6 nm thick and 2 nm thick Au nanodisk in air versus simulated absorbed fraction of 6 nm thick and 2 nm thick Au nanodisk with different particle diameters. a) Solid black line: experimentally measured total absorption for photocathode in air with 6 nm thick Au nanodisks. Colored lines with symbols: simulated total absorbed fraction for a photocathode in water employing a periodic array of 10 nm, 20 nm, and 30 nm diameter gold particles with a separation of 5 nm, 10 nm, and 15 nm respectively. b) Solid black line: experimentally measured total absorption for photocathode in air with 2 nm thick Au nanodisks. Colored lines with symbols: simulated total absorbed fraction for a photocathode in water employing a periodic array of 2 nm, 5 nm, 7 nm, and 10 nm diameter gold particles with a separation of 1 nm, 2.5 nm, 3.5 nm, and 5 nm respectively. The diameters of particles were chosen based on the calculated particle size distribution from SEM characterization.

Figure 2.9b shows the measured total absorbed fraction in air of photocathodes with 2 nm thick Au NPs. The samples with 2 nm thick Au NPs appear brown-reddish in color. The smaller absorbed fraction within the Au NPs is expected from our electromagnetic simulations and could be improved to similar values as for the 6 nm thick Au NPs by adjusting the NiO_x spacer layer thickness to 80 nm (Supporting Information S9). However here we opted to keep the electrical

properties of the two photoelectrode geometries the same and therefore did not alter the NiO_x thickness. The SEM image of 2 nm thick Au NPs (Fig. 2.3.) yields a particle size distribution varying from 2 nm to 20 nm. Generally, as the particles become more isotropic i.e. the aspect ratio of diameter to thickness tends towards unity, the plasmon resonance of the particles will blue-shift. Thus, for a random distribution of particles with diameters ranging from 2 nm to 20 nm and a thickness of 2 nm, the plasmon peaks cover a region from around 600 nm to 900 nm. The strongest plasmon peak is located around 800 nm since nanoparticles with 10 nm diameter have the highest occurrence. In addition smaller particles cause significantly smaller absorption because of their decreased volume.

Experimentally we observed a large broadband absorption feature from 400 nm to 550 nm for the 2 nm thick Au NPs sample which looks somewhat more pronounced than for the 6 nm thick Au NPs, and the 6 nm thick Au NPs sample shows unexpected low absorption around 400 nm. Absorption in this region is due to the inter-band transitions in Au NPs and does not contribute to the generation of electrons that are energetic enough to drive the HER. Again our electromagnetic simulations qualitatively support broadband absorption, and show that no plasmon resonance peak exists below 600 nm, not even for the smallest isotropic Au NPs in our 2 nm thick Au NP samples. We therefore speculate that the small photocurrents that are present in the region from 575 nm to 650 nm for the 2 nm thick Au NPs with diameters in the range from 2-5 nm, but not for the 6 nm thick larger diameter Au NPs, could be due to quantum confinement effects [62, 63].

In summary, a new approach towards plasmon mediated hot-electron generation for solar-to-chemical energy conversion has been presented. The present device is capable of efficient direct hot electron injection for photocatalysis, and the produced photocurrent is similar to that of recent reports[32] for driving the hydrogen evolution reaction, but in contrast to previous designs, the device architecture possesses a relatively small catalytic surface area (basically a planar geometry), it does not utilize expensive platinum as a co-catalyst, it uses a minimum amount of gold, and importantly, it does not rely on a Schottky junction to collect the hot-electrons, thereby opening possibilities for cheaper, simpler and more efficient devices.

Chapter 3: Ultra-thin AAO membrane as a generic template for sub-100 nm nanostructure fabrication [6]

3.1. Introduction

Since pioneering works by Masuda et al. [64] [65], anodic aluminum oxide (AAO) membranes with regularly arrayed of monodisperse pores are well-adopted template for simple and cost-effective, yet high-throughput top-down nanofabrication [66] [67] [68] [69] [70] [71] [72] [73] [74] [75]. Meanwhile, the advantages of nanoimprint lithography has been exploited to further control the shape, size and geometry of the pores [76] [77] [78] [79] [80] [81]. Regarding template-based nanofabrication, alumina membrane possessing adjustable pore and cell size were successfully realized as evaporation mask for nanoarray fabrication mainly on Si substrate [65] [69] [82] [83] [84] [85] [86]. However, nanoarray fabrication with sub-100 nm feature remains challenging due to shadowing effect [69] as it requires ultrathin alumina membrane (UTAM) to minimize the aspect ratio of pores (typically less than 6) for efficient material deposition through the channels [69]. Here the main challenge is proper handling and intact transfer of very fragile UTAM onto substrate of interest. A common practice to address this issue is exploiting a thin supportive layer, normally PMMA (poly (methyl methacrylate)), on UTAM. However, removal of organic layer and transfer of UTAM onto substrate without breaking, cracking, folding and ripping is still problematic. Additionally, organic residues left from dissolving polymeric layer are potential source of surface contamination. Besides, this approach is not applicable to susceptible substrates that are not chemically compatible with utilized organic solvents for removal of organic supportive layer. Because of these issues, nanoarray fabrication with sub-100 nm dots sizes has been mainly restricted to Si substrate [65] [82] [87] because of its chemical compatibilities and very smooth surface.

The latter provides good contact area between attached membrane and the substrate that retains the membrane on the Si surface via Van der Waals interactions or through surface treatment [71]. Lastly, although there have been significant contribution on employing AAO membrane to develop functional nanostructure, the majority of AAO-based device for feasible applications have been fabricated by electrochemical deposition of nanowire and nanorods into long aspect ratio channels with large pore sizes [28 70 88] or developing surface-enhanced Raman scattering (SERS) active substrate through simple material deposition on thick AAO membrane [89] or as-fabricated membrane [90]. On the other hand, applications of AAO-assisted nanoarray have been limited, in particular for nanoarray with sub-100 nm particle size. This can be attributed to difficulties for preparing and transferring UTAM and subsequent efficient material deposition through membrane, surface contaminations from organic residues, and most importantly substrate limitations. The first two concern have been recently addressed by interesting works of Meng et al, [71] and Al Haddad et al., [91]. Meng et al, [71] demonstrated large-scale fabrication of ultrathin AAO free-standing membrane for intact transfer to Si substrate with subsequent sub-100 nm nanoarray fabrication. Here, the authors had to expensive ion milling for barrier layer removing that can also adversely affect underlying substrate. For the work reported by Al Haddad et al., [91] the base Al layer and barrier layer removal was performed after intact transfer of wafer-scale UTAM to the Si substrate. Although the wet chemical etching using $CuCl_2$/HCl solution mixture does not have significant adverse impact on Si substrate, it is very clear that developed technique cannot be applied to general substrate, in particular to susceptible thin film substrate.

Here, a simple strategy is demonstrated for preparing free-standing through-hole UTAMs for efficient sub-100 nm nanoarray fabrication. The approach can be generalized to any substrate

and material. With the help of developed strategy it is possible to fabricate centimeter-scale of plasmonic photocathodes consisting size-controlled dense array of sub-100 nm Au and Ni nanodots on top of very susceptible substrate of NiO_x thin film. In addition, I successfully decorated rough substrates of ~ 940 nm thick FTO (33 nm RMS, about 200 nm peak- peak surface roughness) and ~150 nm thick ITO (0.8 nm RMS, 7 nm peak-peak surface roughness) with highly density of sub-100 nm nanodots array. To test the capability of developed route for efficient nanoarray fabrication on general substrate, a typical plasmonic photocathode consisting sub-50 nm Au nanoarray was applied for direct plasmon-enhanced photoelectrocatalysis. As is demonstrated, the obtained results revealed a great potentials for establishing foundation of AAO-based generic nanoarray fabrication for novel applications.

3.2. Results and Discussions

Figure 3.1a-f depicts graphical illustration for highly ordered nanoarray fabrication on general substrates. This was achieved through developing a simple method for preparing high quality of free-standing thorough-hole UTAM floating on water that subsequently is transferred to the substrate of interest for material deposition. Highly regular UTAM with initial average pore size of 37 nm and interspacing distance of about 100 nm (Fig. 3. 1g) was prepared via a modified two-step anodization of high-purity aluminum foil (99.999%) in 0.3M of oxalic acid [65] [92] (see chapter 4 for details of fabrication process). Prior to etching base Al layer, a thin layer of polystyrene (2 wt% PS/$CHCl_3$) was coated on alumina surface either through spin coating or drop casting. Next, the base remained Al layer was detached in mixture solution of $CuCl_2$/HCl with very low quantity of TX-100 additive to reduce surface tension [93] and small quantity of HNO_3 additive to facilitate dissolution of copper precipitation on UTAM. During etching process and afterward the UTAM was handled using plastic strainer. The barrier layer removing and

pore-opening process was carried out using a 5% H_3PO_4 at room temperature for different time period to obtain through-hole UTAM with different pore diameters. Then, the film was rinsed with DI and was left on strainer to be dried. Usually after etching base aluminum layer, some large-sized Al residues are left at the bottom of AAO membrane that makes nanofabrication process less efficient in particular on rough substrates. To solve this issue, it is possible to flip the film, before removing polymeric layer, such that the face of UTAM with smoother feature from electropolishing in first step is placed on substrate.

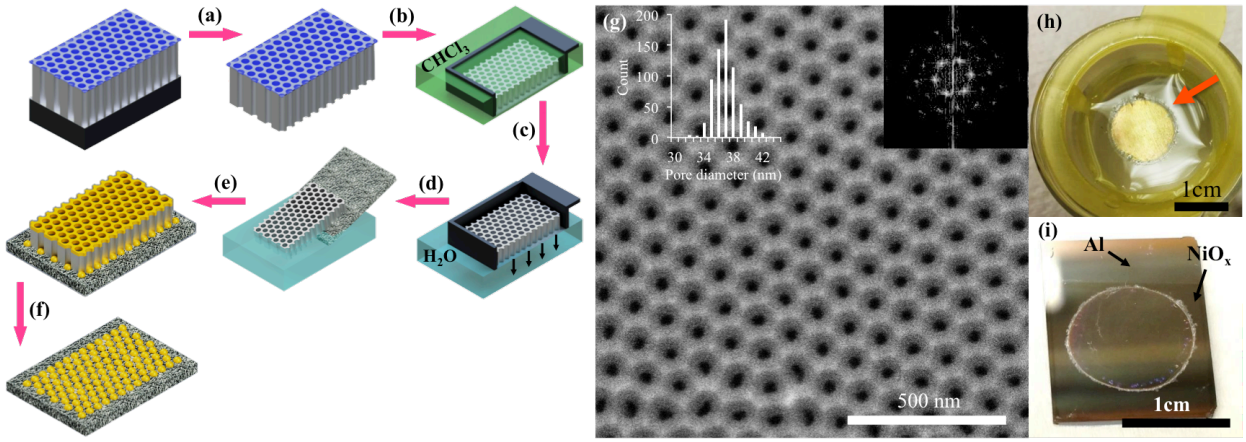

Figure 3.1. a-f) schematic of preparing free-standing UTAM and subsequent intact transfer to substrate of interest for nanoarray fabrication. a) etching underlying Al layer and pore opening b) removing polystyrene layer in chloroform c) Floating UTAM on water d) transfer of UTAM onto general substrate e) material deposition f) removal of UTAM. g) SEM image of as-fabricated UTAM on Al. The initial average pore size is about 37 nm with periodicity of about 100 nm. The FFT result shows perfect hexagonal arrangement of the pores. h) Digital image of a free-standing UTAM with sub-300 nm thickness floating on water. i) Intact transfer of UTAM to the substrate consisting 40 nm thick NiO_x thin film prepared on Al/Si.

The next step is removing PS layer for that a few ml of chloroform gently dropped on the film supported by strainer. This is followed by entire immersion of UTAM in chloroform for

about 10 min to obtain clean membrane without any organic residues. After complete evaporation of the solvent, the strainer gently pushed against water, where surface tension pushes the UTAM upward results in detachment of membrane from strainer and floating on water (Figure 3. 1c, h). The floating UTAM can be perfectly transferred to substrate of interest (Figure 3. 1d, i) even without performing any surface treatment. Experimentally, it was observed that leaving the sample in tilted angle after transfer process helps for faster drying and better adhesion of membrane to substrate because while the water slowly leaves the sample the membrane is stretched and sticks perfectly to the underlying substrate. Heating the sample is not recommended as it leads twisting, folding and cracks in membrane. As an alternative strategy, the through-hole UTAM was supported by retained Al frame at the edges UTAM (Fig. 3. 2.). Here the polymer layer was completely removed by immersion of sample in $CHCl_3$ after barrier layer removal in H_3PO_4.

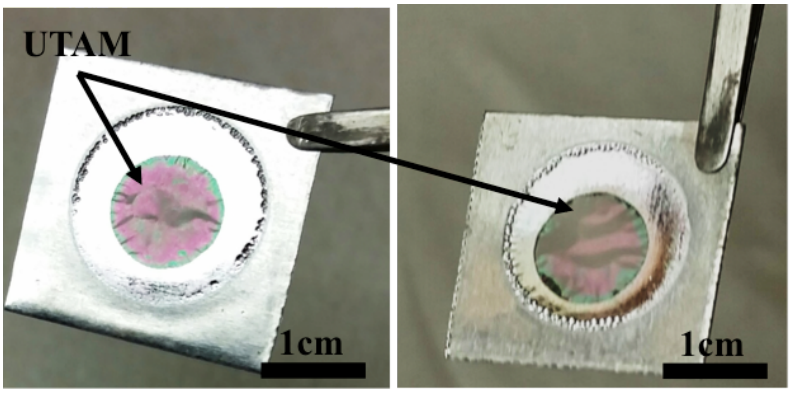

Figure 3.2. Digital images of free-standing thorough-hole UTAMs (~300 nm thick) supported by original Al frame at the edges.

Similar approach was previously shown to be efficient for transferring large-scale UTAM to surface treated Si substrate [71] although expensive ion milling had to be employed for barrier layer removing and membrane thinning. However, ion milling can adversely affect underlying

substrate, in particular the NiO_x thin films under study. In addition, we observed more efficient UTAM transfer onto substrates for transfer process carried out in water. Strong adhesion of UTAM to substrate is essential for its application as an evaporation mask. It is worthy to mention that polymer coating not only impede breaking or ripping UTAM during etching process in erosive etching solution, it also limits H_3PO_4 to only etch the bottom surface of the barrier layer that is crucial for controlling pore size [87]. In fact, we also performed Al etching process on unsupported UTAM in saturated $CuCl_2$ solution followed by removing Al residuals in $CuCl_2$ and HCl mixture as highlighted in previous work [81]. However, preparing centimeter scale of free standing sub-300 nm thick AAO was not productive as for most of cases the AAO broke, cracked, or sunk in solution in addition to observing uncontrolled pore opening.

Figure 3. 1i shows digital image of the UTAM placed on 40 nm thick NiO_x film prepared on highly reflective substrate of Aluminum. The scanning electron microscopy (SEM) images of the UTAM (Figure 3. 3a) shows that the membrane is quite thin with a thickness of about 220 nm. UTAM was utilized as an evaporation mask for nanoarray on top of NiO_x. Figure 3. 3b shows an array of Au nanodots on NiO_x surface obtained from evaporation of 15 nm Au on UTAM. As can be seen, the pore regularity has been successfully transferred to the nanodots on substrate. Most of particles are in the range of 40 nm to 57 nm with an average diameter of ~ 50 nm. From SEM image, the dots does not have perfect spherical cross-section. Such a broad particles distribution and distortion of shape of particles should be attributed to the misalignments of the hole with the incident Au beam from evaporation source that was placed in more than 50 cm distance from the sample in our evaporation set up. In addition, the deviation could be due to distortion of ideal circularity of the pores at bottom side of membrane during barrier layer removing in H_3PO_4 [94]. In order to obtain particles with ideal circular cross-section,

we mildly annealed the sample in 400C at air and interestingly found that the particles adopted an ideal shape alongside more than 10 nm decrease in average particle diameter and narrower size distribution (Figure 3. 3c). In the other word, after annealing the particle diameter reduced to 36 nm (± 4 nm) with consistent average inter-particle distance of about ca. 64 nm. As expected, such a significant decrease in particle diameter was accompanied with an increase in particles height. According to figure 2d the average height of the dots after annealing increased to 30 nm. Rough calculations showed that increasing the particle height to almost twice of its original height in here is in agreement with about 10 nm decrease in particle diameter assuming the same volume for particles. The low-magnified SEM images of the sample before and after annealing (Fig. 3.4.) revealed that the ordered nanodots are arranged in uniform interval with excellent density on surface (ca. 1×10^{10} cm^{-2}) throughout SEM micrograph.

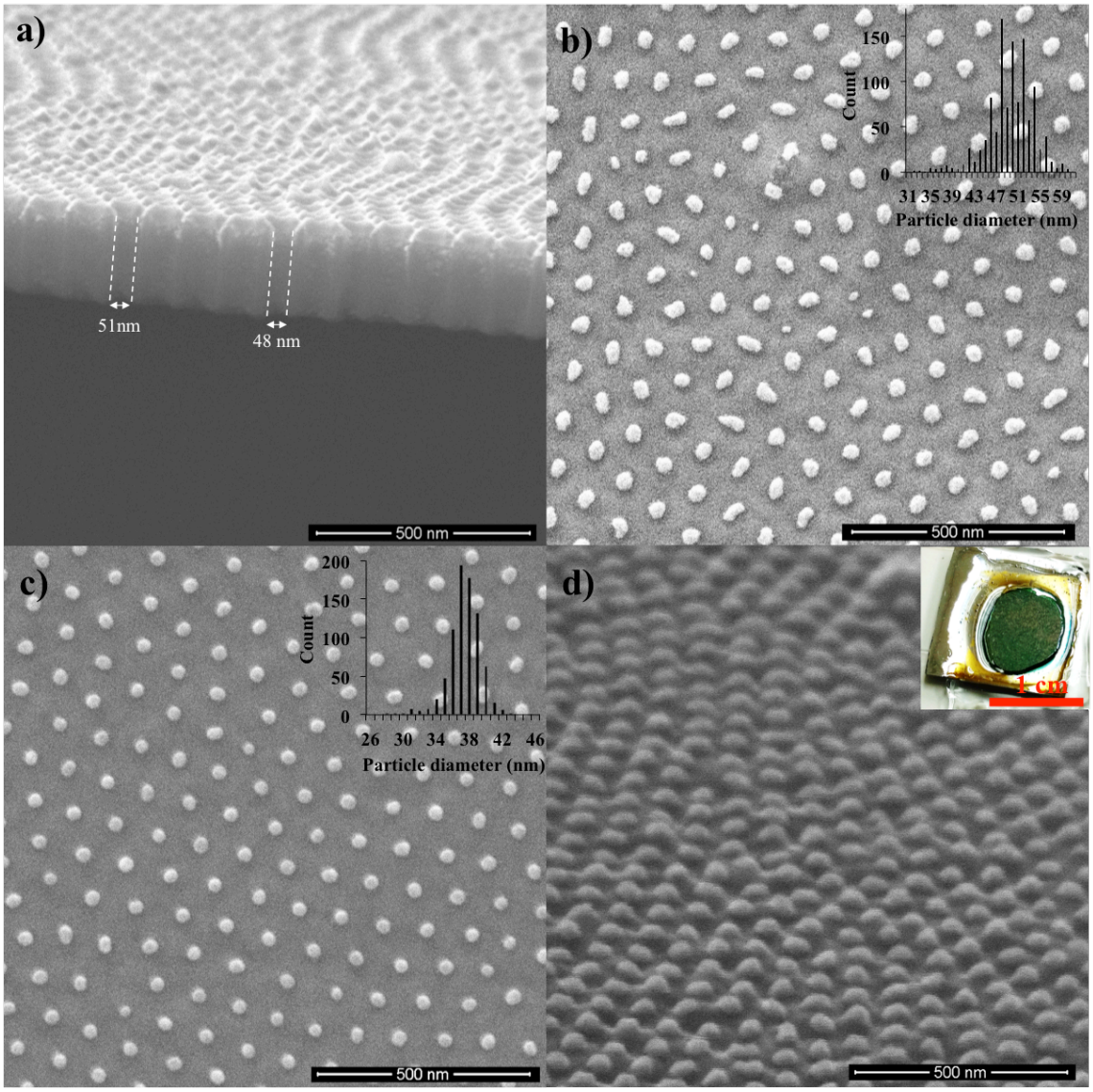

Figure 3.3. Fabrication of highly-ordered Au nanodots array on NiO_x with high-density of particles and controlling particle geometry. a) Cross-sectional SEM image of UTAM with sub-250 nm thickness placed on 40 nm NiO_x layer. b) NiO_x surface patterned with highly-ordered Au nanodots array with average particles size of 49 nm through evaporation of 15 nm Au on UTAM. c) Formation of nanodots with ideal spherical cross-section through annealing the pristine sample (b) for 2 hr in 400C at air. After annealing, nanodots adopted the ideal shape with spherical cross-section accompanied by more than 10 nm decrease in particles diameter. d) Oblique-view of the sample after annealing shows average height of 30 nm for nanodots. Inset in d is digital image of the sample after annealing.

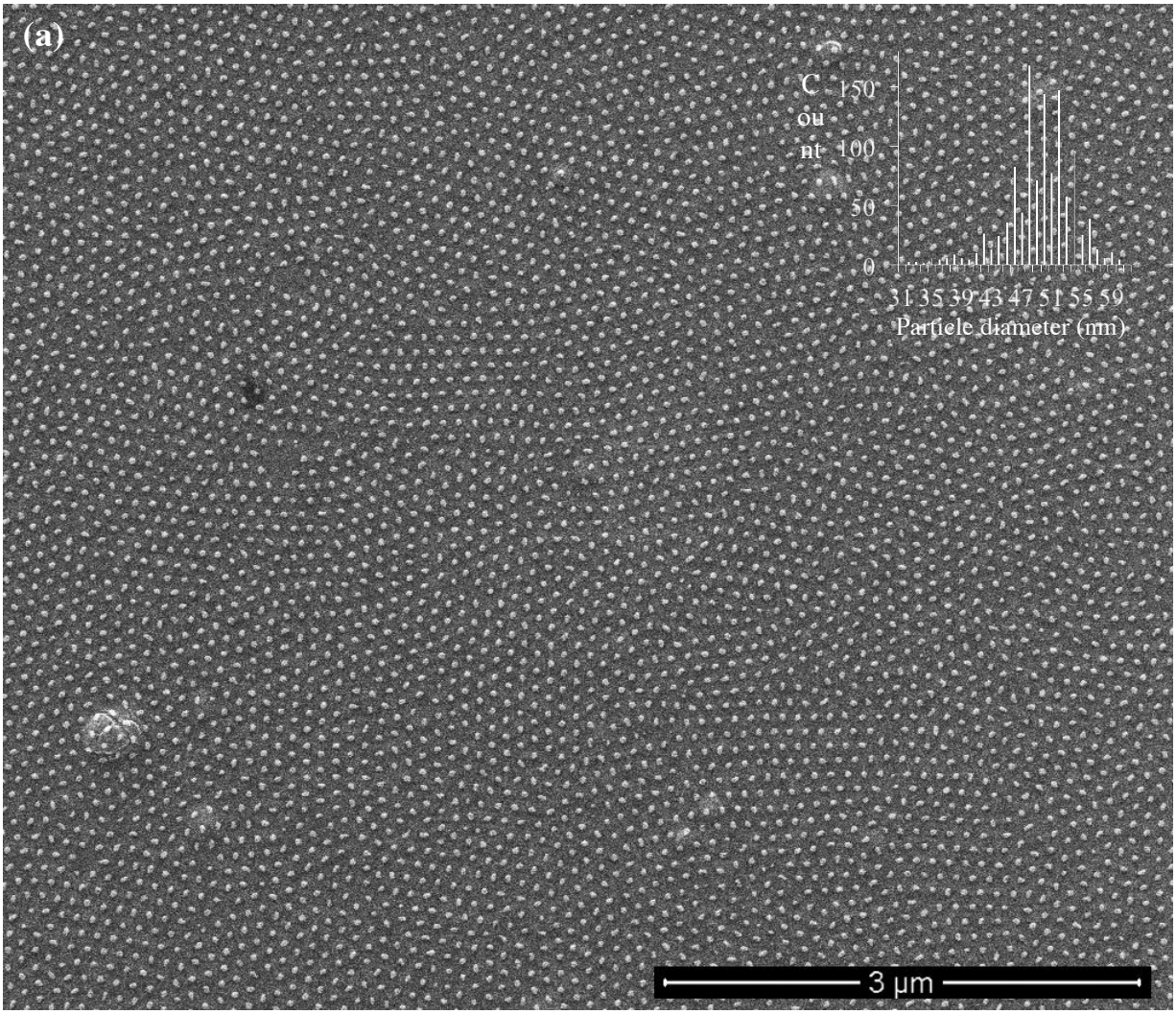
(a)
Count
150
100
50
0
31 35 39 43 47 51 55 59
Particle diameter (nm)
3 µm

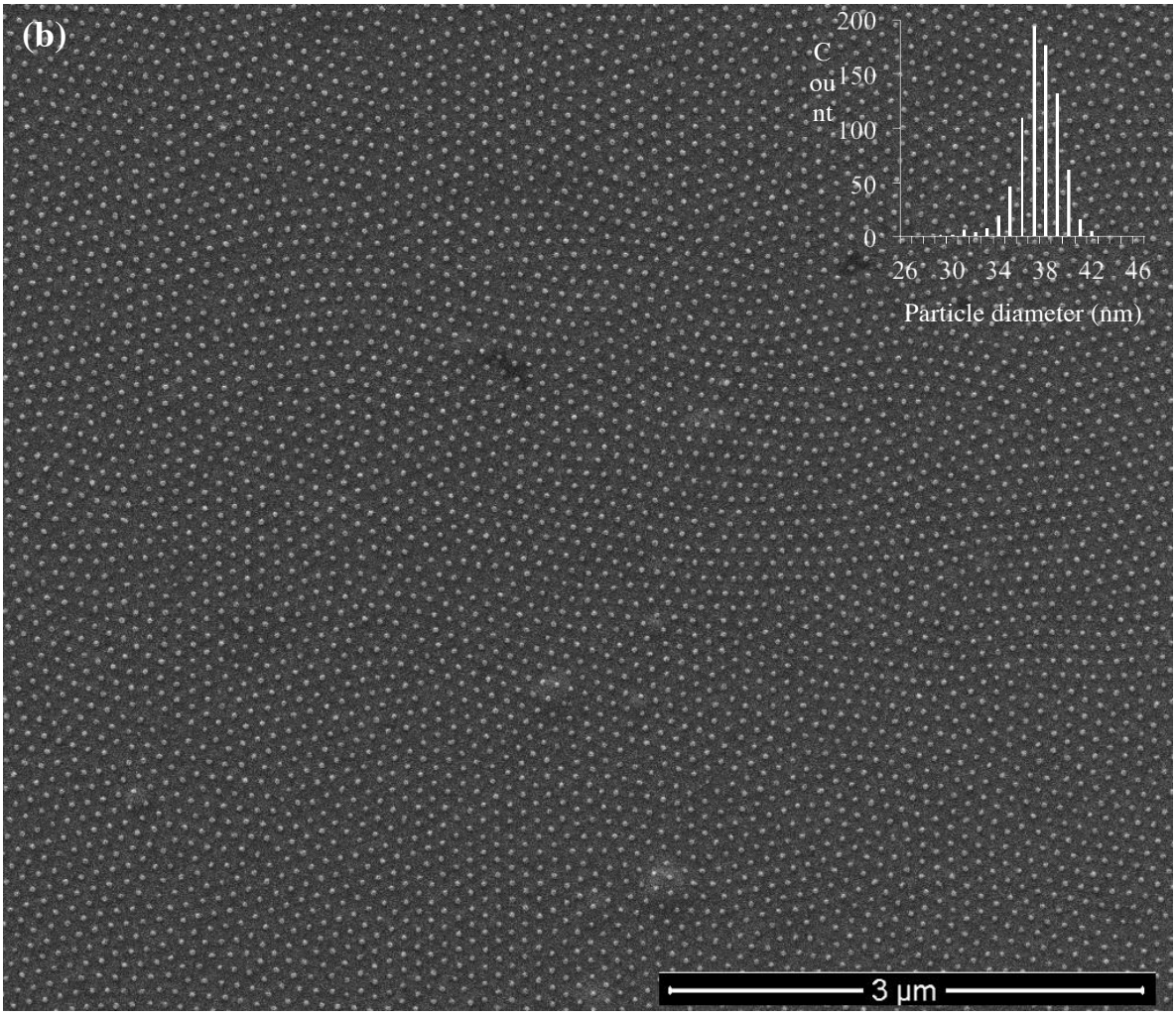
(b)
200
C
ou
nt
150
100
50
0
26
30
34
38
42
46
Particle diameter (nm)
3 µm

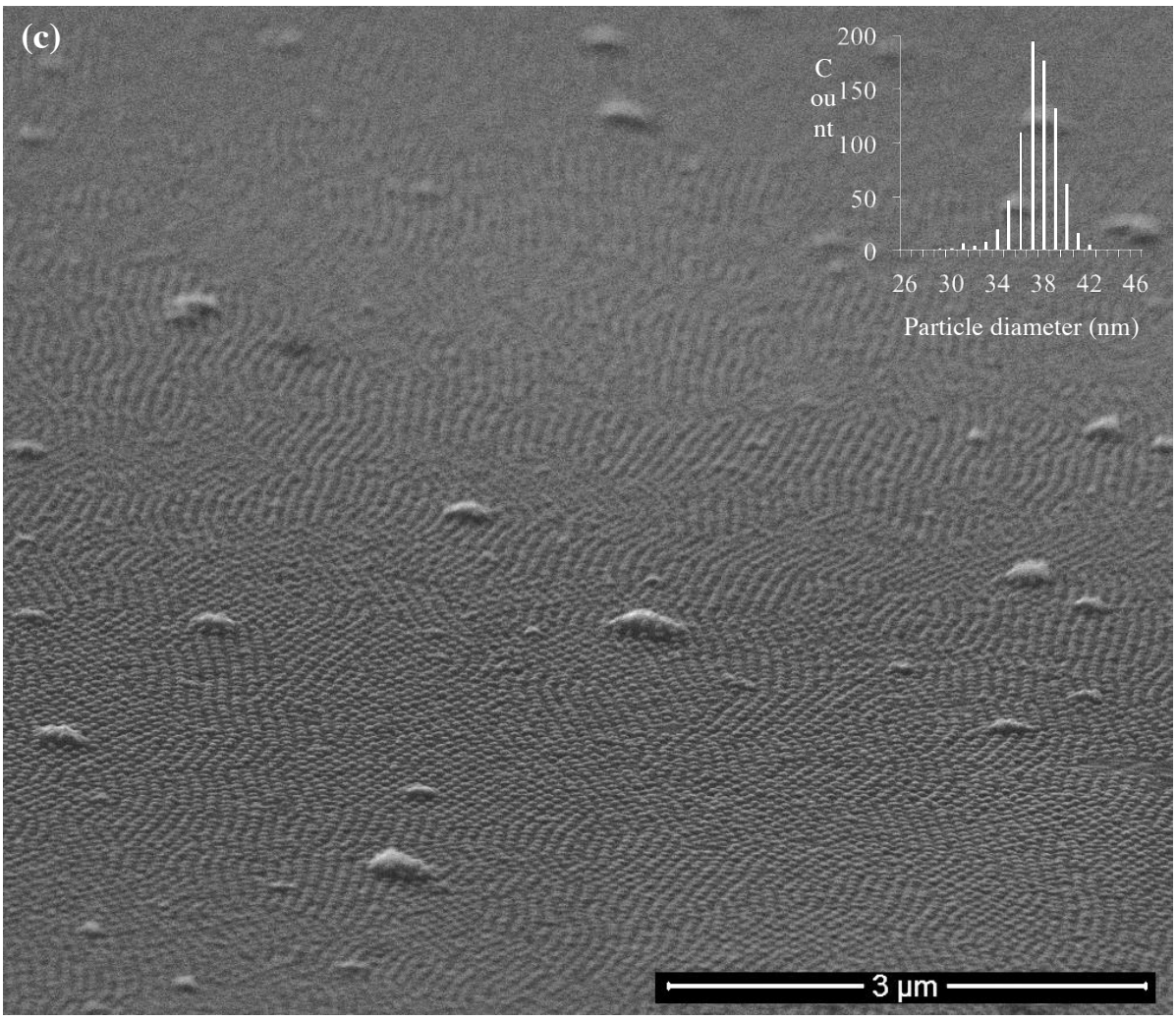

Figure 3.4. Large area SEM images of plasmonic photocathode consisting highly-ordered Au nanodots showing high density of nanodots on top of 40 nm NiO_x. (a) Top-view image of nanodots before annealing (see Fig. 3.3b) with average particles size, thickness and periodicity of 49nm, 15nm, and 100 nm, respectively. Top-view (b) and oblique-view (c) images of nanodots after annealing the sample at 400C in air (see Fig. 3.4). The average particles size, thickness and periodicity are 36nm, 30nm, and 100 nm, respectively.

The size of nanodots were further controlled through controlling pore sizes in H_3PO_4. Figure 3. 5. shows highly-ordered array of nanodots with average diameters of ca. 48 nm, 64 nm, and 80 nm, and corresponding inter-particle distance of ca. 52 nm, 36 nm, and 20 nm fabricated on 40 nm NiO_x via evaporation of 20 nm Au on UTAM. The large-area SEM images (Figure 3.6 – 3.7.) evidently show uniform interval, narrow size distribution (± 5nm), and excellent density of highly ordered dots on NiO_x surface to the point that even bumps on underlying NiO_x Layer with a few hundred-nm heights are decorated with nanodots.

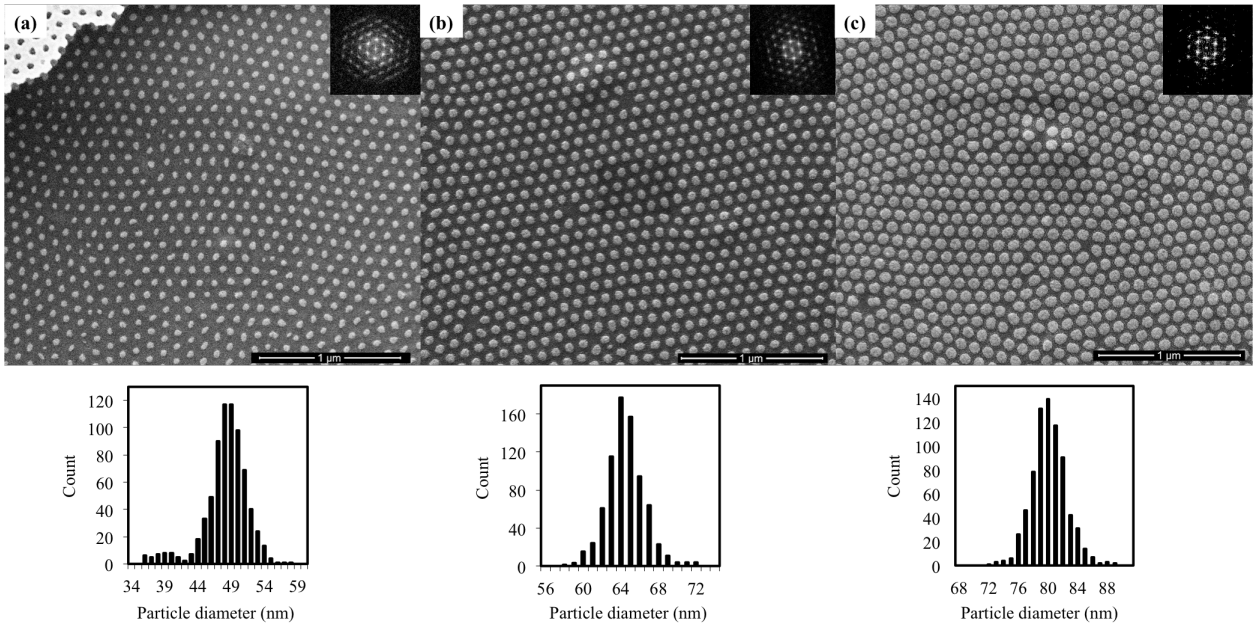

Figure 3.5. Size-controlled fabrication of highly-ordered sub-100 nm Au nanoarray on NiO_x surface. From a to c, the average particles size are 48nm, 64nm, and 80 nm respectively. For all samples, the particles thickness and periodicity were 20nm, and 100nm, respectively.

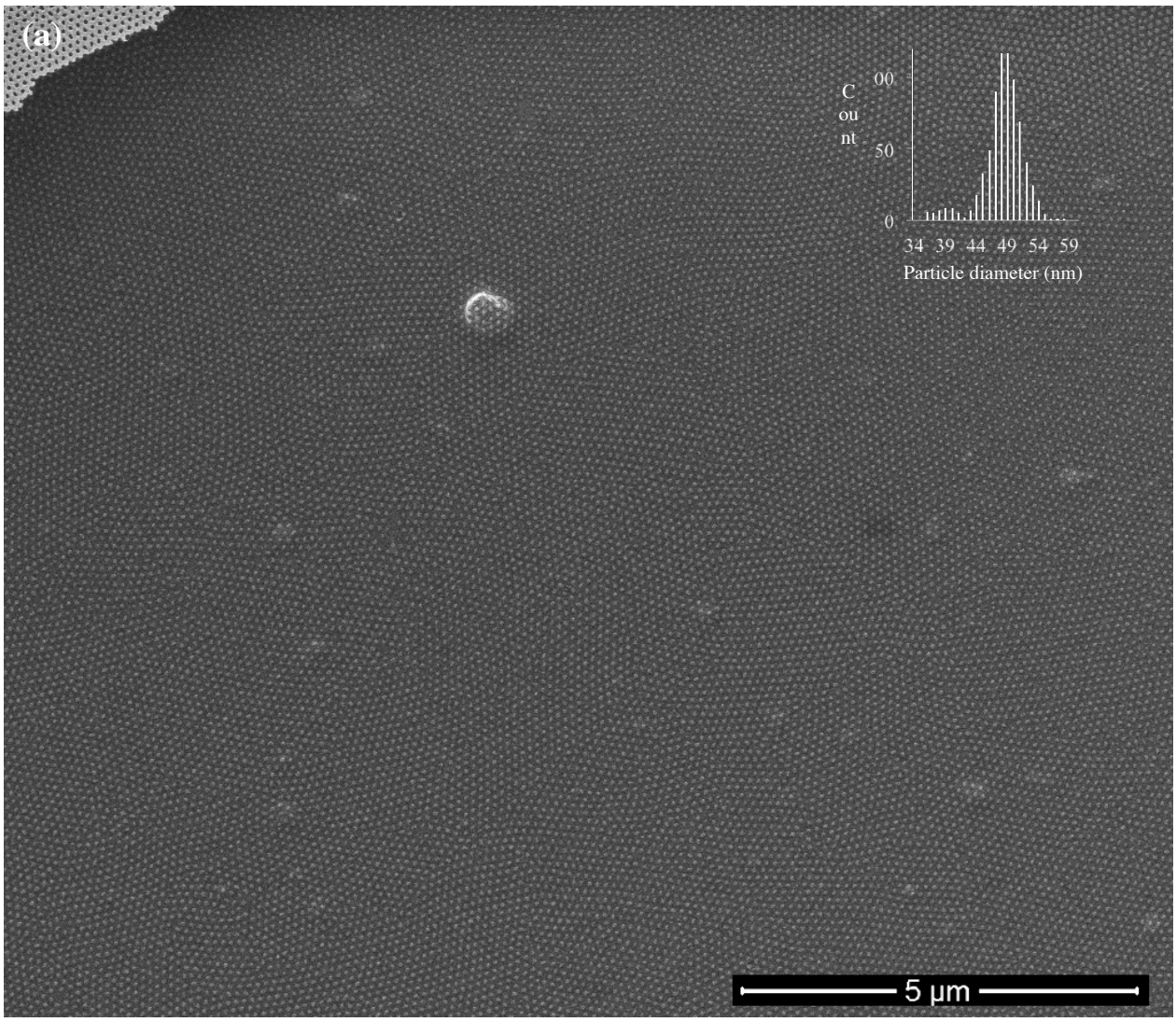
(a)
C
ou
nt
00
50
0
34 39 44 49 54 59
Particle diameter (nm)
5 µm

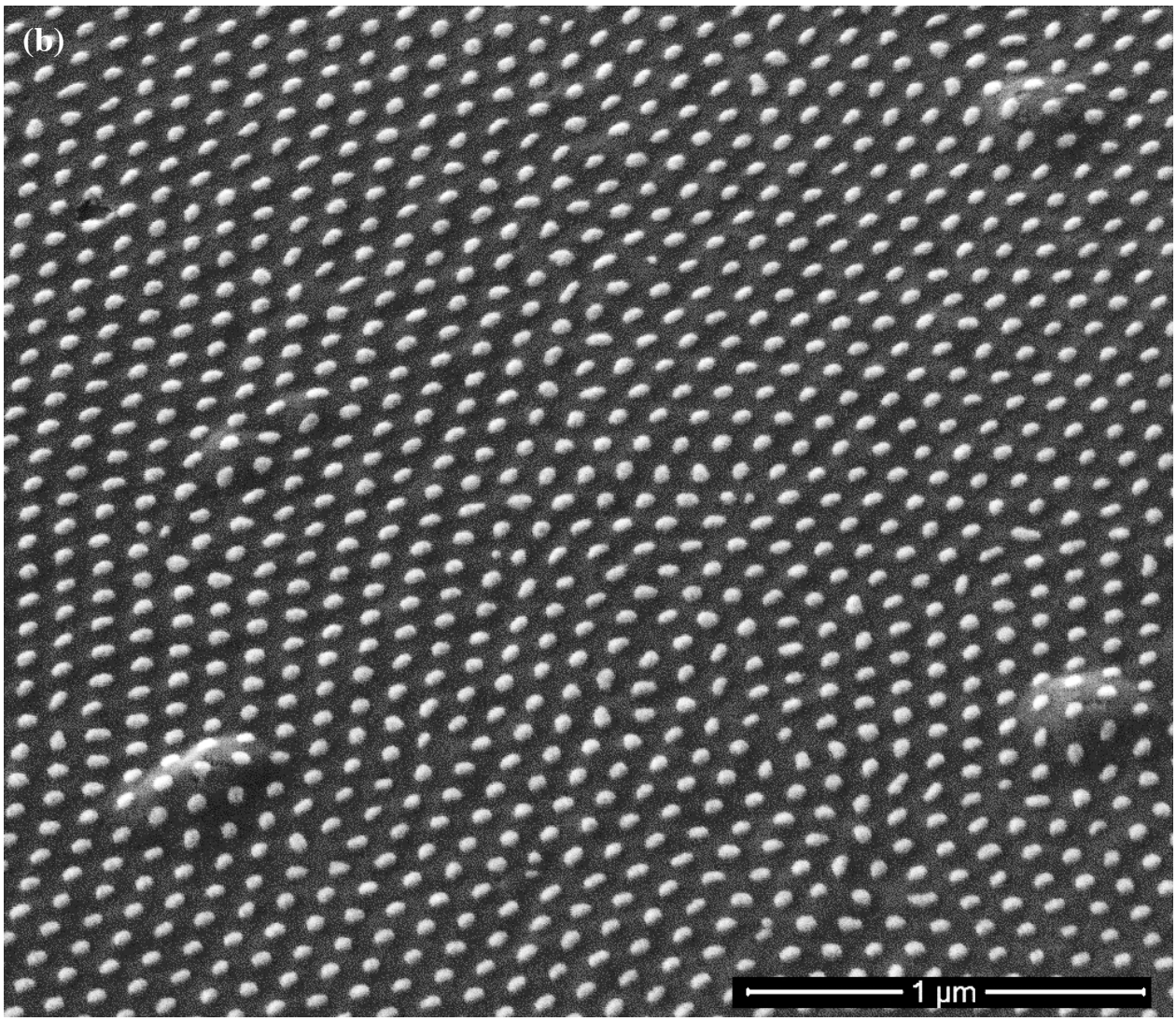

Figure 3.6. (a) Top-view and (b) oblique-view of large area SEM image of plasmonic photocathode from consisting ordered arrays of sub-100 nm Au nanodots on top of 40 nm NiO_x layer. The average particles size, thickness and periodicity are 48 nm, 20 nm, and 100 nm, respectively (also see Fig. 3.5a). Interestingly, even small bumps from underlying NiO_x layer with a few hundred nm heights were decorated with nanodots that indicate the quality of UTAM transfer to the substrate.

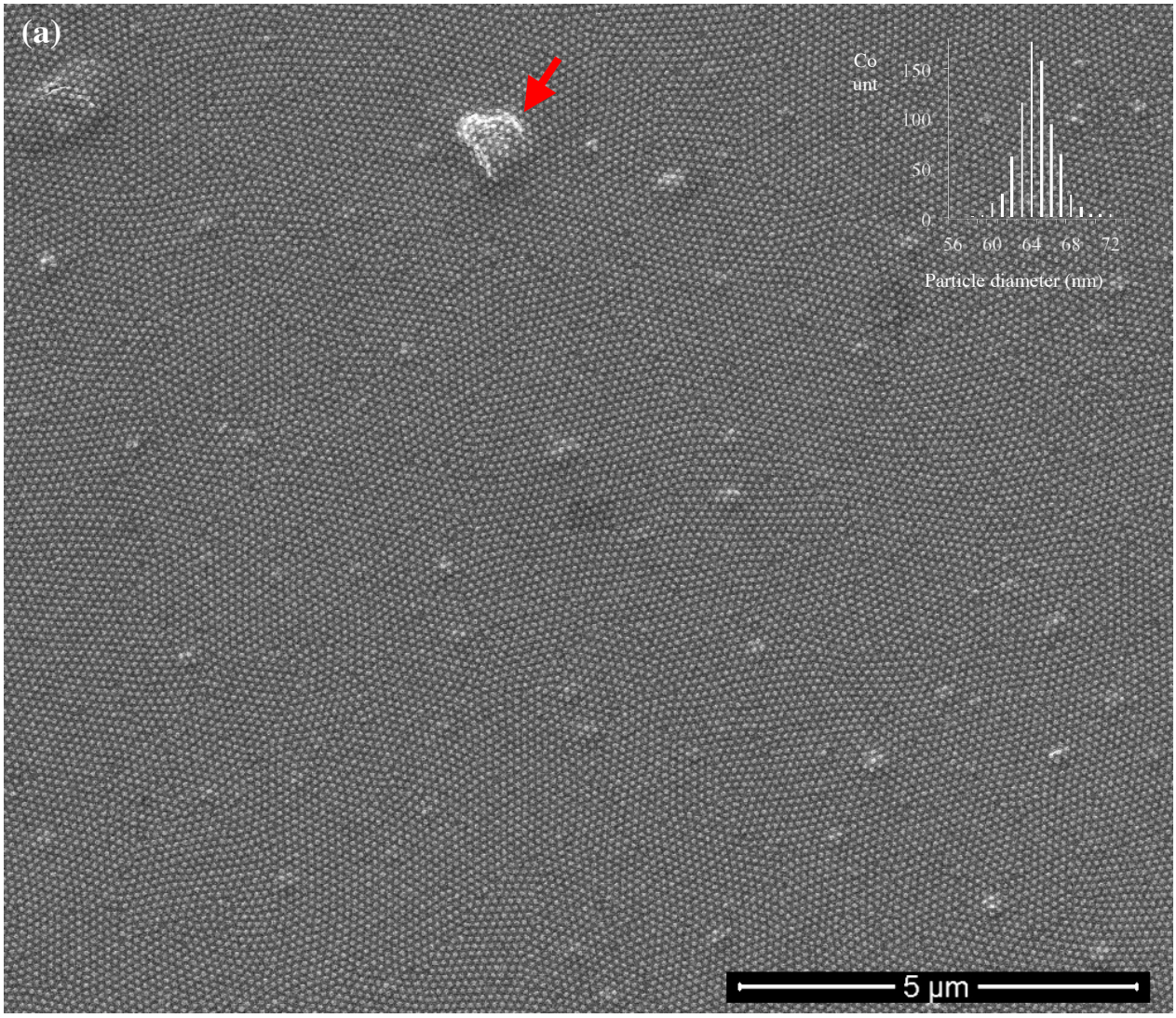
(a)
Co
unt
150
100
50
0
56
60
64
68
72
Particle diameter (nm)
5 μm

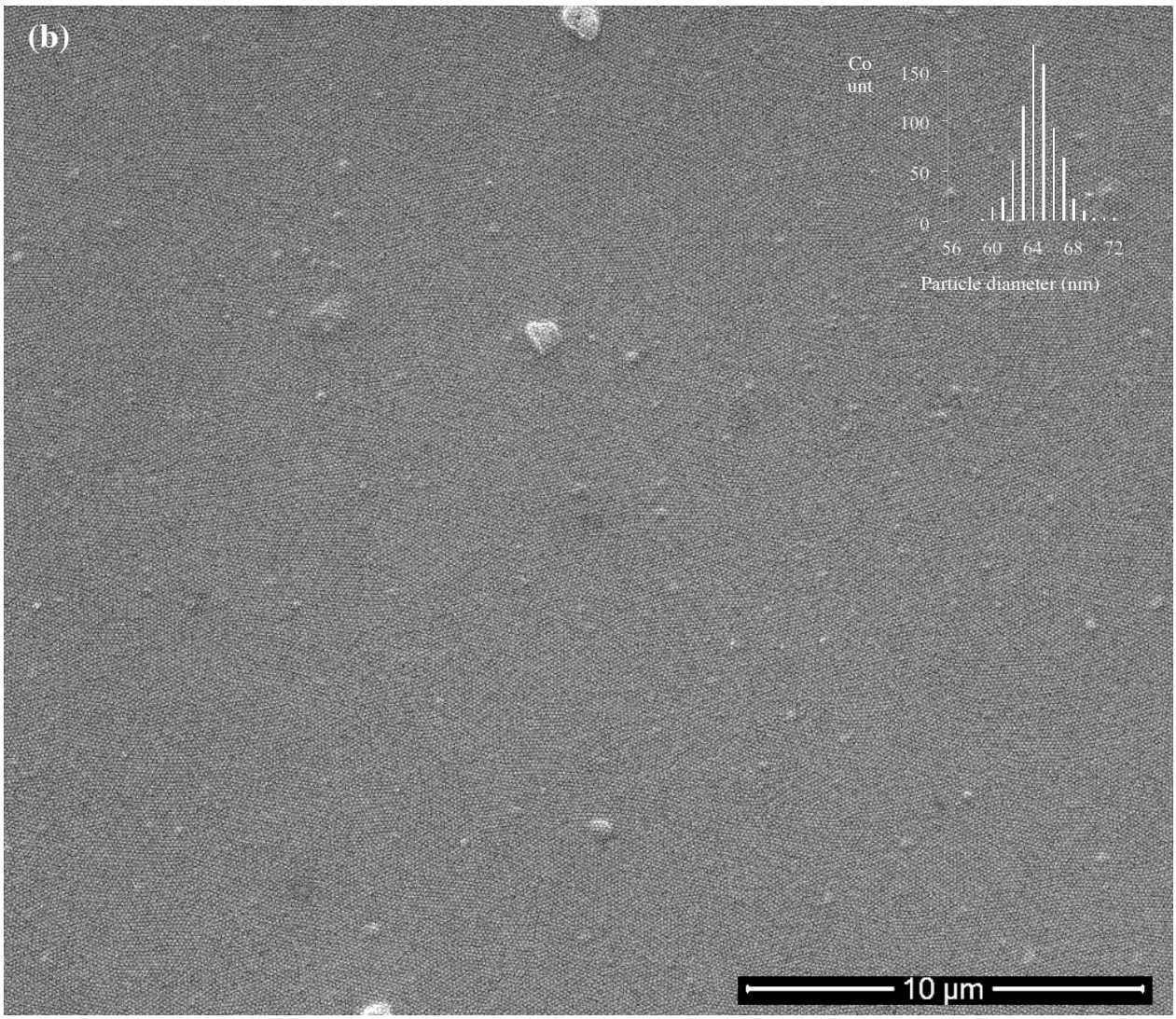

Figure 3.7. (a) and (b) top-view large area SEM image with different magnification from plasmonic photocathode consisting ordered arrays of sub-100 nm Au nanodots on top of NiO_x layer. The average particles size, thickness and periodicity are 64nm, 20nm, and 100 nm, respectively (also see Fig. 3.5b). Both images represent excellent density of nanodots on surface. In particular figure (b) shows complete coverage of nanodots with almost zero number of missing dots in arrays. This indicates the capability of developed strategy for prefect, yet neat, transfer of UTAM transfer to the substrate of interest for subsequent sub-100 nm nanoarray fabrication.

In addition, the possibility of controlling the size of particle size through mild annealing process was investigated for the initial evaporation thickness of 5 nm of gold. After the annealing, interesting nanoarray structure consisting single, dimer, trimer or even pentamer of nanodots was found with sub-10 nm gaps and particles size in the range of 5nm to 30 nm. (Figure 3.8.). Further adjustment of evaporation thickness can be taken for precise control of particles size to develop interesting structures for novel applications.

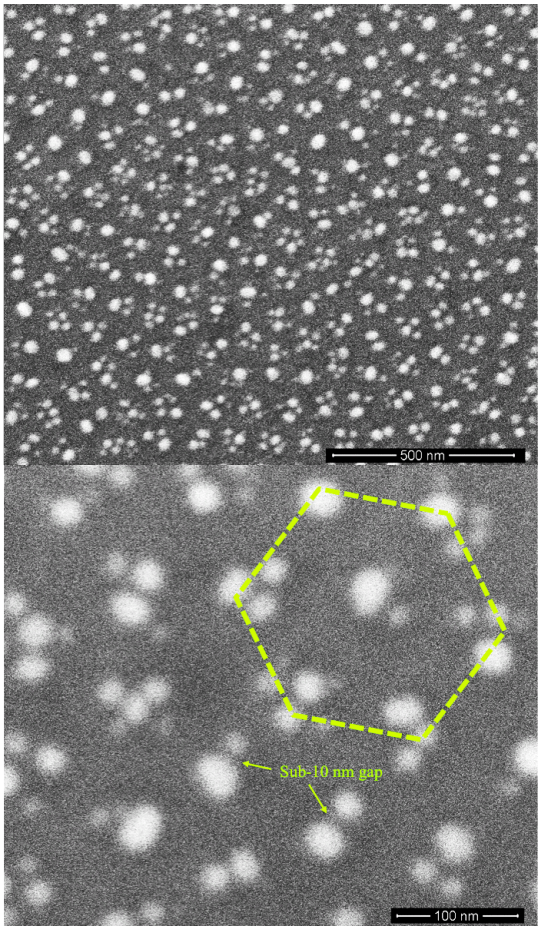

Figure 3.8. Top-view SEM image of interesting plasmonic nanoarray structure consisting single, dimer, trimer or even pentamer of nanodots in the range of 5nm to 30 nm with sub-10 nm gaps fabricated on top of NiO_x layer from evaporation of 5 nm Au through UTAM and annealing afterwards.

At this stage, Au mainly was utilized to demonstrate nanoarray fabrication on non-siliconic substrate. But, the developed strategy is a pragmatic approach to apply AAO-based nanoarray fabrication to any material and substrate. To end this, the developed strategy was extended for nanoarray fabrication using nickel nanodots on NiO_x surface. Exploring plasmonic properties of nickel nanoantennas is emerging as a very attractive area of research due to its distinct plasmonic features combined with strong magnetic properties [95]. Figure 3. 9a shows SEM image of nickel nanodots array with sub-100 nm particle diameter on NiO_x surface. Recent works were shown importance of nanostructured metal oxides (NMOs) as a promising building block in fabrication of biosensor [96]. Therefore, such a Ni nanodots/NiO_x structure might open up the pathway to design advanced nanoplasmonic biosensor devices for improving sensing characteristics while it can be remotely controlled by external magnetic fields. Next, we examined the versatility of the developed methodology for nanoarray fabrication on rough substrates of ~ 940 nm thick FTO (33 nm RMS, about 200 nm peak- peak surface roughness) and ~150 nm thick ITO (0.8 nm RMS, 7 nm peak-peak surface roughness) of FTO and ITO. Figure 3. 9b shows a typical UTAM with thicknesses of about 122 nm transferred onto ~ 940 nm thick FTO, while the underlying substrate is beautifully visible. As mentioned before, it is observed several micron-sized Al residual on backside of UTAM that impede efficient transfer of UTAM to rough substrate. However, it is possible to circumvent this problem by flipping the AAO/polymer film, before removing polymer layer, such that its smoother face was ultimately placed on the substrate. Then a randomly chosen thickness of 10 nm and 15 nm of Au were deposited on FTO, and ITO, respectively. As can be seen in Figure 3. 9c-d, both substrates were successfully patterned by dense arrays of hexagonal arranged sub-50 nm particles.

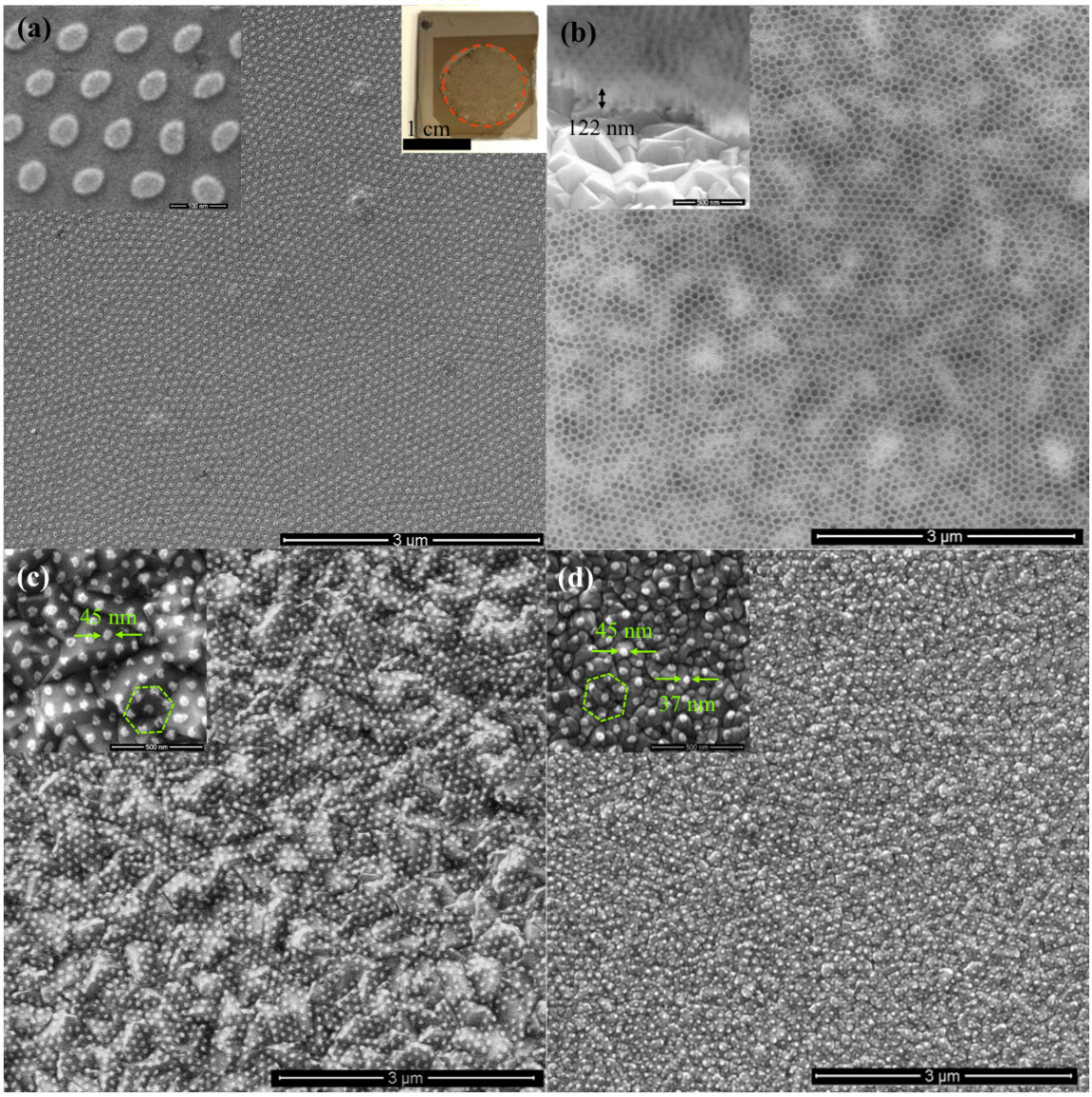

Figure 3.9. Exploiting the capabilities of developed methodology for extending nanoarray fabrication to different material and substrates. a) Fabrication of sub-100 nm nickel nanodots array on 40 nm NiO_x/Al/Si substrate through evaporation of 20 nm nickel on UTAM. b) Plain-view and oblique-view SEM image of typical UTAM (122 nm thick) successfully transferred onto very rough substrate of ~ 940 nm thick FTO (33 nm RMS, about 200 nm peak- peak surface roughness) for subsequent nanoarray fabrication. c,d) Dense Au nanoarray with sub-50 nm particles size fabricated through evaporation of 10 nm Au on UTAM/FTO **(c)** and 15 nm on UTAM/ITO (0.8 nm RMS, 7 nm peak- peak surface roughness) **(d)** substrates.

Here it is worthy to emphasize on importance of preserving the quality of underlying substrate during nanoarray fabrication. To investigate that, the nanoarray fabrication on NiO_x substrate was carried out according to routinely used method for removing organic layer after the UTAM/organic layer is placed on substrate. Unfortunately, there is considerable damage to underlying NiO_x layer caused by $CHCl_3$ solvent (Figure 3. 10). In addition, significant decrease in density of particles was observed that should be ascribed to micron-sized polymer residues left on UTAM, which prevent material deposition into the channel.

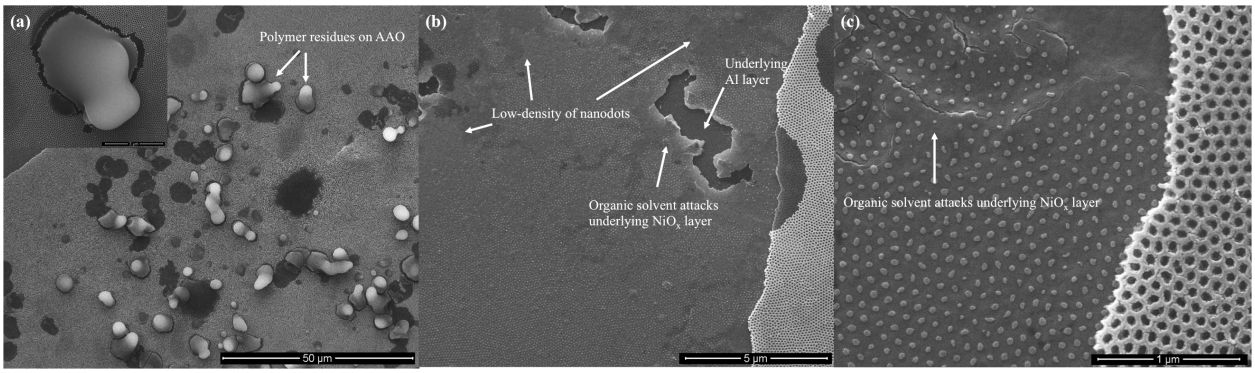

Figure 3.10. Au nanoarray fabrication on NiO_x substrate was conducted through direct transfer of UTAM/PS film onto 40 nm NiO_x layer on Al and subsequent removal of PS layer from UTAM while the membrane was placed on substrate. As can be seen, there is considerable damage to underlying NiO_x layer induced by $CHCl_3$ solvent. In addition, significant decrease in density of particles was observed that should be ascribed to micron-sized polymer residues left on UTAM, which prevent material deposition into the channel.

Recent years have witnessed intensive interest of implementing plasmonic nanostructures for enhancing the efficiency of light-harvesting devices both for photovoltaic [97] [98] [56] and photocatalysis applications [3] [14] [20] [21] [42] [99]. Recently, plasmonic hot-carrier generation from the non-radiative surface plasmon decay has been exploited as a novel approach for solar-to-fuel energy conversion [2] [26] [32] as it promises to open up novel photoreduction pathways that are inaccessible by conventional methods such as heating or applying an electrochemical bias. In this regard, we recently presented a novel plasmonic photoelectrode architecture consisting of high density of gold nanoparticles for direct plasmon-driven photoelectrocatalysis of water through efficient hot-electrons generation and injection into adsorbed molecules from a Schottky junction-free device [4] (also see Chapter 2 of this thesis).

Herein, a typical plasmonic photocathode was used for direct hot-electron induced solar water splitting to assess performance of developed strategy for feasible applications. Figure 3.11 illustrates plasmonic photoelectrode structure, consisting of plasmonic nanodots array in direct contact with water. The main difference between current device and the device in chapter 2 is in employing well-fabricated highly ordered Au nanodots array in instead of randomly oriented anisotropic particles. Again, NiO_x is regarded as a selective spacer layer with its exclusive electrical and optical functions. The electronic function of the NiO_x layer is to confine generated hot electrons within the nanoparticles while allowing for hole transport to the aluminum back electrode and further through the external circuit to the platinum counter electrode. The optical function of NiO_x is to serve as a highly transparent wide bandgap spacer layer between the plasmonic nanodots and the Aluminum back reflector for maximum light absorption within the nanoparticles. In addition, NiO_x acts as a high-refractive index substrate ($n \sim 2.3$) that can enhance the coupling of light into the substrate over a broad spectral range [100].

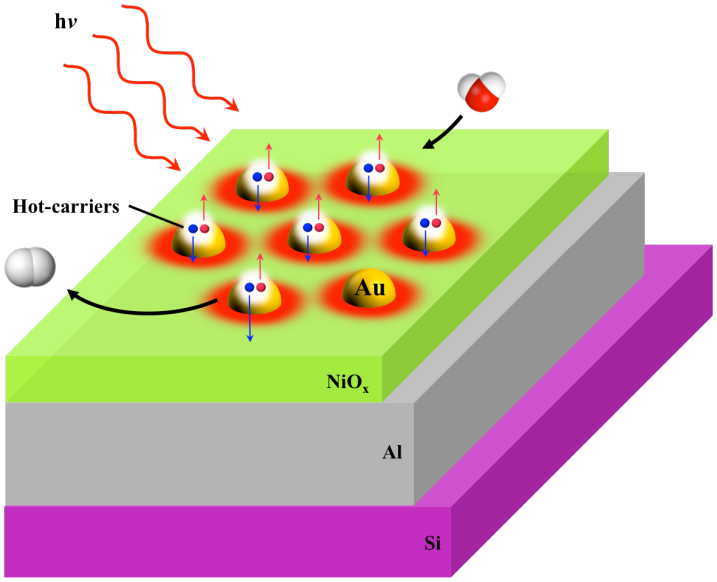

Figure 3.11. Structure of the highly ordered plasmonic photocathode nanoarray for plasmon mediated direct hot electron injection from a Schottky junction-free device to drive solar-to-chemical energy conversion.

Figure 3.12 shows experimentally measured total absorbed fraction in air for versus simulated absorbed fraction in Au and simulated total absorbed fraction in air for photocathode consisting Au nanodots with average diameter of 36 nm and 30 nm thick, and 100 nm center-to-center particle distances on 40 nm NiO_x layer (sample from Fig. 3.3d). As can be seen the experimentally measured total absorption faithfully matches with simulation result in terms of absorption pattern and plasmon resonance frequency. In compare with our previous study on randomly oriented anisotropic particles with heterogeneous size distribution and broad plasmon resonance absorption, the plasmonic photocathode in here exhibit a distinct plasmon resonance peak at 650 nm as the well-shaped nanodots are arranged in ordered array with homogenous (narrow) particle distribution.

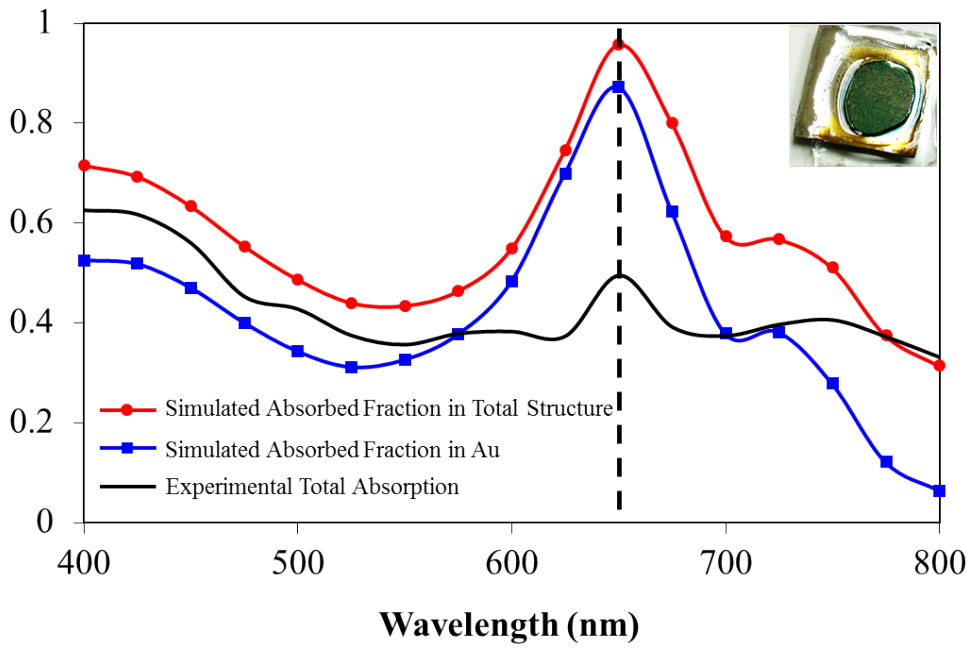

Figure 3.12. Experimentally measured total absorbed fraction in air versus simulated absorbed fraction in Au and simulated total absorbed fraction in air for photocathode consisting Au nanodots with average diameter of 37 nm and 30 nm thick, and 100 nm center-to-center particle distances on 40 nm NiO_x layer. The experimentally observed plasmon resonance at 650 nm faithfully matches with simulation results.

The numerical absorbed fraction in Au and total absorbed fraction reaches about 85% and 95%, respectively, at plasmon resonance while the observed total absorption is about 50%. Further adjustment of the spacer layer thickness can allow for achieving maximum absorption close to unity within the gold nanoparticles based on electromagnetic simulations (Figure 3.13.). However, the thickness of NiO_x film was kept on 40 nm for the sake of comparison with our previous study on randomly distributed particles. As expected, the both experimentally measured total absorption and simulated absorbed fraction within the Au nanodots show increased absorption at wavelengths below 550 nm due to interband transitions from the occupied d-band.

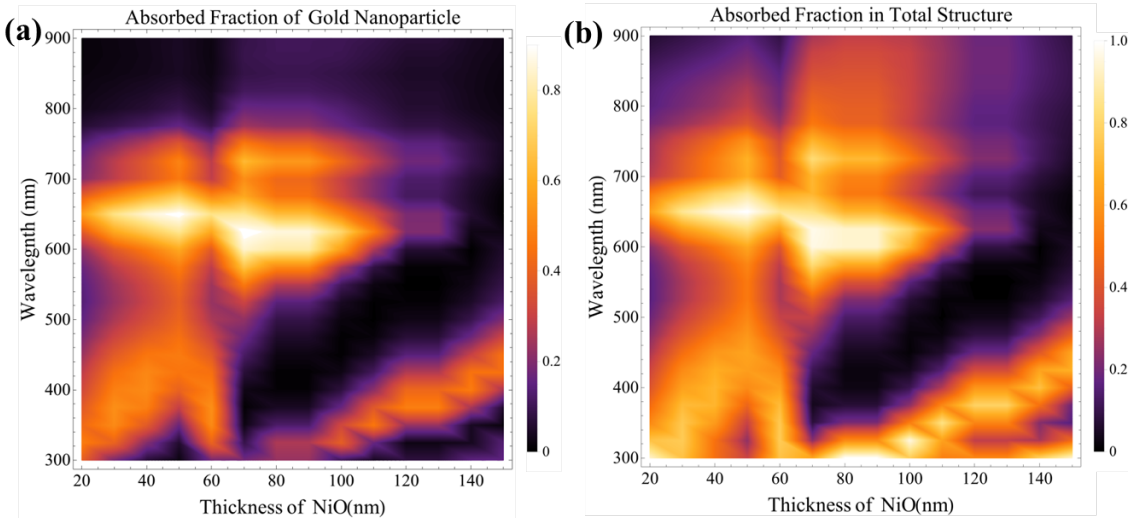

Figure 3.13. Simulated absorbed fraction of light within (a) Au NPs (average diameter of 37 nm and 30 nm thick, and 100 nm center-to-center particle distances) and (b) total structure versus thickness of NiO_x. For a 40 nm NiO_x spacer layer thickness, the numerical absorbed fraction only in gold and total absorbed fraction within photocathode structure reaches about 85% and 95%, respectively.

The energy schematic of the photoelectrode structure is similar to that of previous structure using random nanoparticles except for having different plasmon excitation frequency. Here for device architecture consisting highly ordered nanoarray, plasmon excitation happens at around 650 nm, there fore the energy of plasmon-induced hot electron is ~1.9 eV at most. As the redox potential for HER lies at excitation energy of about ~1 eV above the Fermi energy of the Au, hot electrons with energies greater than ~1 eV plus the required overpotential should be able to transfer directly into the unoccupied states of the reactant species and thus result in the initiation of the photocatalytic HER. Similarly, as we observed for our previous device (Fig. 2. 4a), the photoexcited carrier due interband transition are not energetic enough to drive HER as the upper edge of d-band is located ~ 2.3 eV below Fermi level of Au [101] and therefore for optical excitation with wavelength of above 400 nm (maximum energy of ~ 3.1 eV) the electrons

excited from d-band are typically promoted to unoccupied states near the Fermi level or maximum ~ 0.8 eV above Fermi level.

Figure 3.14a, shows linear sweep voltammetry measurement of plasmonic photocathode decorated with Au dots nanoarray having 36 nm (± 4 nm) diameter and 30 nm height (Fig. 3.3c,d) under chopped illumination at about one sun (100 mW/cm^2) immersed in a nitrogen-purged solution of 0.5 M Na_2SO_4 buffered at pH 5.0. Photoelectrochemical measurements were performed in a cell with a three-electrode configuration where Ag/AgCl (in sat. 3.0 M KCl) and a Pt mesh were the reference and the counter electrode, respectively. The onset photocurrent at 0.4 V vs RHE is approximately 0.35 μA/cm^2 that reaches 8.2 μA/cm^2 at zero overpotential versus the RHE. The cyclic voltammogram of the plasmonic photocathode under chopped light showed consistent photocurrents according to applied biases (Figure 3. 15b). The observed photocurrents are less than that of device with randomly distributed particles (Figure 2. 4b, 2. 7). This can be explained based on lower fill fraction of nanoparticles along with larger particle sizes for the case of nanoarray device. However, the photocurrents extracted from nanoarray of particles are still on a par with a recently demonstrated large catalytic surface area of Pt/TiO_2/Au nanorod array Schottky junction geometry for HER [32]. The control experiment for NiO_x/Al sample without Au nanodots (inset Fig. 3.14) shows a photocurrent of about 0.25 μA/cm^2 at an electrode potential of 0V vs. RHE. In the other words, the photocurrent from presence of Au nanodots array is ~35x larger.

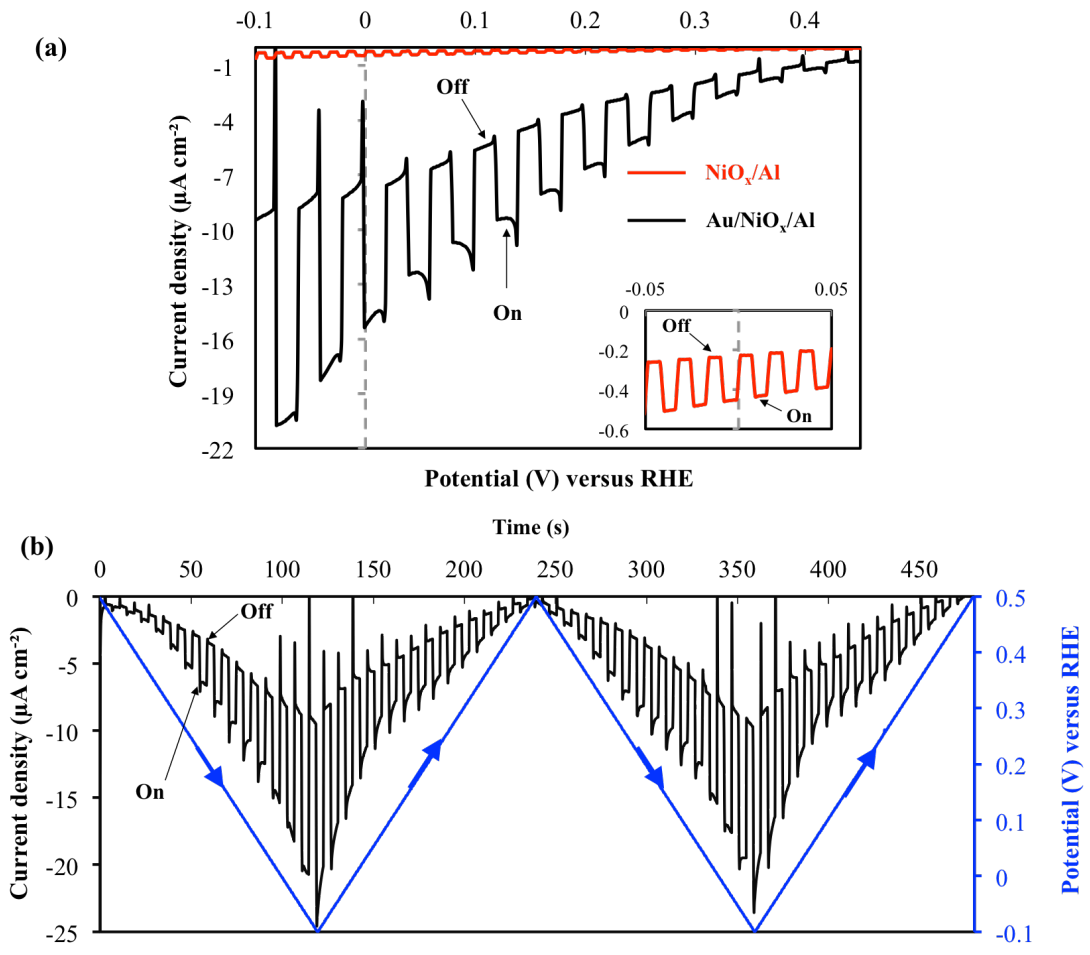

Figure 3.14. Photoelectrocatalytic performance of the plasmonic photocathode decorated with Au dots nanoarray having 36 nm (± 4 nm) diameter and 30 nm height. (a) Linear sweep voltammetry (LSV) measurement under chopped illumination at about one sun (100 mW/cm^2) immersed in a nitrogen-purged solution of 0.5 M Na_2SO_4 buffered at pH 5.0. The red line is control experiment for sample without Au nanodots. (b) The cyclic voltammogram of the plasmonic photocathode under chopped light showed consistent photocurrents according to applied biases. The photocurrent was measured in a three-electrode photoelectrochemical cell configuration with a Pt mesh as the counter electrode, and is plotted versus the reference hydrogen electrode (RHE).

In summary, a simple strategy for efficient nanoarray fabrication on general substrates was presented based on UTAM. In this regard, plasmonic nanoarray consisting sub-100 nm nanodots were fabricated on various substrates, including NiO_x thin film, very rough FTO and ITO substrates. The capability of developed methodology for fabrication of photocatalytic devices has been presented through direct application of a typical plasmonic photocathode consisting sub-50 nm nanodots array toward plasmon mediated hot-electron injection from a Schottky junction-free device to water molecules for solar-to-chemical energy conversion. This work can provide the impetus for AAO-based fabrication of novel nanoarray on general substrates that consequently can expand implementation of nanoarray in several fields, such as photovoltaic, photocatalysis, nanophotonics and spectroscopy, as well.

Chapter 4: Experimental and methods

NiO_x thin film preparation: The precursor sol-gel of NiO_x was prepared according to existing procedures with minor modifications [59]. 0.2M nickel (II) diacetate tetrahydrate (≥99.0% $Ni(AC)_2.4H_2O$, Sigma-Aldrich®) was dissolved in a 9:1 solution mixture of dimethylethanol amine (≥99.0% dmaeH, Sigma-Aldrich®) / mono-ethanol amine (≥98.0% MEA, Sigma-Aldrich®), and refluxed for about 4 hours at 100°C. After cooling to room temperature, the as prepared sol-gel with dark blue color was filtered (Anodisc 0.2micron) and aged 24 hours at room temperature before usage. A NiO_x film with thickness of about 40 nm was prepared by spin-coating at 4000 rpm for 15 seconds (Laurell model WS-650MZ-23NPP-Lite) followed by drying the sample on a hotplate at 275°C for 15 minutes with subsequent sintering at 400°C in air at one atmosphere in the tube furnace (Mellen SC12.5R).

Formation of random particles on substrate: prior to evaporation of a gold film on top of the NiO_x surface, an oxygen plasma treatment was performed for about 5 minutes (200 W oxygen plasma cleaner) to clean and ensure decomposition of organics in the NiO_x layer. E-beam evaporation of a 2 nm, 6 nm, and 10 nm thick film of gold was performed at a base pressure of about 5×10^{-6} torr and a constant deposition rate of 0.1 Å/s. Then, the sample was annealed in air at one atmosphere in the tube furnace. During the annealing process, the temperature was raised from room temperature to 300 °C within 30 minutes, was held constant for one hour, and naturally cooled down to room temperature.

Fabrication of ultrathin free-standing Anodized Aluminium Oxide (AAO) mask and transfer process: Anodized aluminium oxide (AAO) mask with initial pore size of 37 nm and interpore-distance of 100nm was fabricated through two-step anodizing procedure [65] [71]. High purity Aluminum foil (99.999%, thickness of 0.25 mm, Sigma Aldrich) was first annealed at 400C for

about 2hr and degreased with acetone/methanol mixture. This was followed by electropolishing of Al foil at 20V in a vigorously stirred solution of 1:4 (V/V) perchloric acid (78%) and ethanol (99.99%) at 1°C for about 1min. The average current density during electropolishing process was about 60mA. First anodization step was performed at 0.3M Oxalic acid, 40V, 1°C for more than 12hr. The preliminary oxidized layer was removed in the solution mixture of H_3PO_4 (6wt %) and CrO_3 (1.8%) at 80°C for about 4hr. The second anodization was carried out at the same condition for less than 3 minutes in order to fabricate ultrathin alumina membrane (UTAM) with typical thickness of sub-300nm. Next, a thin layer of polystyrene (2 wt% PS/$CHCl_3$) was coated on UTAM either by spin coating or drop casting to support UTAM during etching the base aluminum substrate. The sample was then left for 10 min with subsequent heating at 100C to evaporate the solvent. Here we utilized PS, instead of PMMA, as it is easier and faster to be removed without leaving major residues behind.

Material deposition through UTAM: Deposition of Au and Ni on UTAM were performed using regular e-beam evaporation system where the distance between source and sample was more than 50 cm. During evaporation process, the base pressure was kept between 10^{-5}-10^{-6} torr with the deposition rate constantly controlled at 0.2 Å/s.

Photoelectrochemical measurements: all photoelectrochemical and spectral photocurrent measurements of the fabricated plasmonic photocathodes were taken in a three-electrode photoelectrochemical cell setup with a Ag/AgCl (in 3.4 M KCl) reference electrode, a Pt mesh counter electrode, and with a SP-300 potentiostat (Bio-Logic Science Instruments, USA) with LabVIEW version 2011. All measurements were carried out at room temperature and in 0.5 M Na_2SO_4 (trace metal basis, Alfa Aesar) buffered at pH 5.2 using a phosphate buffer (phosphoric acid (ACS grade EMD), potassium monohydrogen phosphate (99.99% Sigma-Aldrich®).

Aqueous solutions were prepared with ultra-pure water (resistivity 18 MΩ.cm) from a Milli-Q water purifier. All electrochemical potentials are reported with respect to the reversible hydrogen electrode (RHE) by using the equation:

$E_{RHE} = 0.205 + E_{Ag/AgCl} + 0.059*pH$

Nitrogen gas was bubbled through the electrolyte solution 30 minutes prior to the measurements, and during the measurements the headspace above the electrolyte solution was continuously purged with nitrogen gas. Electrochemical Impedance Spectroscopy (EIS) was performed with an AC amplitude of 10 mV and a frequency range from 10 Hz to 50 kHz in the same supporting electrolyte solution. For irradiation of the photocathode, a home-built solar simulator equipped with a 1000W Xenon lamp, long pass filters (305 nm, 570 nm and 1000 nm), and a monochromator (Newport) provides a continuously tunable light source from 350 nm to 950 nm with a measured 25 nm full width at half maximum (FWHM). The intensity and spectral shape of the solar simulator output were recorded using a thermal power meter and spectrometer (AvaSpec-2048-USB2), respectively.

Absorption measurement: for absorption measurements a 60 mm plano-convex lens (Thorlabs) was utilized to focus the light to a spot size of 3 mm in diameter. The reflected/transmitted light was collected using an IS200 integrating sphere along with an IS236A Silicon photodetector (350 nm to 1100 nm). Since our fabricated structure has no transmittance, all data were taken in reflection mode and the absorbed fraction versus wavelength was derived from the reflectance data.

Electromagnetic simulation: the Finite Difference TimType equation here.e Domain Method was used to analyze the optical response of the nanostructure. Particularly, we employed the commercial grade software Lumerical FDTD Solutions [102], which is a 3D Maxwell solver

capable of analyzing the interaction of UV, visible, and IR radiation with complicated structures and nanometer scale features. Using Lumerical, an array of Au nanoparticles was simulated, and we investigated the absorption properties in the 300 nm to 950 nm wavelength regime. For the simulation of asymmetrically-shaped nanoparticles with planer geometry in chapter 2, the thickness of the particles was set at the evaporation thickness while the diameter was taken from the measured histogram of particle size distributions. In the simulation, the polarization of the E-field was set along the X-axis and the polarization of the H-field was set along the Y-axis. The propagation direction of light was set along Z-axis. To simulate an array of nanoparticles, symmetric boundary conditions are applied along the X and Y axes. To attain convergence, a Perfectly Matched Layer (PML) condition was applied at the positive Z axis, at 1000 nm above the (x, y, 0) surface. A PML at the Negative Z-axis, starting at -1000 nm, was extended through the structure (in this case Aluminum) for better absorption of light. Hence, the total length of the simulation region along the Z-axis is 2000 nm. A plane wave was launched downward from 100 nm below the upper PML.

REFERENCES

1. Moskovits, M., The case for plasmon-derived hot carrier devices. *Nat. Nanotechnol.* **2015,** *10* (1).
2. Brongersma, M. L.; Halas, N. J.; Nordlander, P., Plasmon-induced hot carrier science and technology. *Nat. Nanotechnol.* **2015,** *10* (1), 25-34.
3. Linic, S.; Christopher, P.; Ingram, D. B., Plasmonic-metal nanostructures for efficient conversion of solar to chemical energy. *Nat. Mater.* **2011,** *10* (12), 911-921.
4. Robatjazi, H.; Bahauddin, S. M.; Doiron, C.; Thomann, I., Direct Plasmon-Driven Photoelectrocatalysis. *Nano Letters* **2015,** *15* (9), 6155-6161.
5. Hägglund, C.; Zeltzer, G.; Ruiz, R.; **Thomann, I.**; Lee, H.-B.-R.; Brongersma, M. L.; Bent, S. F., Self-Assembly Based Plasmonic Arrays Tuned by Atomic Layer Deposition for Extreme Visible Light Absorption. *Nano Lett.* **2013,** *13* (7), 3352-3357.
6. Robatjazi, H., Bahauddin, S. M., Macfarlan, L. H., Fu, S., Thomann, I., Ultra-thin AAO membrane as a generic template for sub-100 nm nanostructure fabrication. *Chem. Mater. (Revised)* **2016**.
7. Patil, R. A.; Devan, R. S.; Lin, J.-H.; Liou, Y.; Ma, Y.-R., An efficient methodology for measurement of the average electrical properties of single one-dimensional NiO nanorods. *Sci. Rep.* **2013,** *3*.
8. Peck, M. A.; Langell, M. A., Comparison of Nanoscaled and Bulk NiO Structural and Environmental Characteristics by XRD, XAFS, and XPS. *Chem. Mater.* **2012,** *24* (23), 4483-4490.
9. Irwin, M. D.; Servaites, J. D.; Buchholz, D. B.; Leever, B. J.; Liu, J.; Emery, J. D.; Zhang, M.; Song, J.-H.; Durstock, M. F.; Freeman, A. J.; Bedzyk, M. J.; Hersam, M. C.; Chang, R. P. H.; Ratner, M. A.; Marks, T. J., Structural and Electrical Functionality of NiO Interfacial Films in Bulk Heterojunction Organic Solar Cells. *Chem. Mater.* **2011,** *23* (8), 2218-2226.
10. Bijith, D. M.; Babu, J.; Vinay, K. G., Photo-conversion of CO2 using titanium dioxide: enhancements by plasmonic and co-catalytic nanoparticles. *Nanotechnology* **2013,** *24* (40), 405402.
11. Cushing, S. K.; Li, J.; Meng, F.; Senty, T. R.; Suri, S.; Zhi, M.; Li, M.; Bristow, A. D.; Wu, N., Photocatalytic Activity Enhanced by Plasmonic Resonant Energy Transfer from Metal to Semiconductor. *J. Am. Chem. Soc.* **2012,** *134* (36), 15033-15041.
12. Torimoto, T.; Horibe, H.; Kameyama, T.; Okazaki, K.-i.; Ikeda, S.; Matsumura, M.; Ishikawa, A.; Ishihara, H., Plasmon-Enhanced Photocatalytic Activity of Cadmium Sulfide Nanoparticle Immobilized on Silica-Coated Gold Particles. *J Phys Chem Lett* **2011,** *2* (16), 2057-2062.
13. Christopher, P.; Xin, H.; Linic, S., Visible-light-enhanced catalytic oxidation reactions on plasmonic silver nanostructures. *Nat. Chem.* **2011,** *3* (6), 467-472.
14. Kale, M. J.; Avanesian, T.; Christopher, P., Direct Photocatalysis by Plasmonic Nanostructures. *ACS Catalysis* **2014,** *4* (1), 116-128.
15. Ingram, D. B.; Linic, S., Water Splitting on Composite Plasmonic-Metal/Semiconductor Photoelectrodes: Evidence for Selective Plasmon-Induced Formation of Charge Carriers near the Semiconductor Surface. *J. Am. Chem. Soc.* **2011,** *133* (14), 5202-5205.
16. Wei She, Z., Liu, S., Low, M., Zhang, S-Y., Liu, Z., Mlayah, A., Han, M-Y. , Janus Au-TiO2 Photocatalysts with Strong Localization of Plasmonic Near-Fields for Efficient Visible-Light Hydrogen Generation. *Adv. Mater.* **2012,** *24*, 2310-2314.

17. Warren, S. C.; Thimsen, E., Plasmonic solar water splitting. *Energy Environ. Sci.* **2012,** *5* (1), 5133-5146.
18. Hou, W. a. C., S. B. , A Review of Surface Plasmon Resonance-Enhanced Photocatalysis. . *Adv. Funct. Mater.* **2013,** (23), 1612-1619.
19. Zhang, X., Chen, Y., Liu, R-S., & Tsai, D. P. , Plasmonic photocatalysis. *Rep Prog Phys* **2013,** *76*, 046401.
20. Thomann, I.; Pinaud, B. A.; Chen, Z.; Clemens, B. M.; Jaramillo, T. F.; Brongersma, M. L., Plasmon Enhanced Solar-to-Fuel Energy Conversion. *Nano Lett.* **2011,** *11* (8), 3440-3446.
21. Liu, Z.; Hou, W.; Pavaskar, P.; Aykol, M.; Cronin, S. B., Plasmon Resonant Enhancement of Photocatalytic Water Splitting Under Visible Illumination. *Nano Lett.* **2011,** *11* (3), 1111-1116.
22. Hou, W.; Hung, W. H.; Pavaskar, P.; Goeppert, A.; Aykol, M.; Cronin, S. B., Photocatalytic Conversion of CO2 to Hydrocarbon Fuels via Plasmon-Enhanced Absorption and Metallic Interband Transitions. *ACS Catal.* **2011,** *1* (8), 929-936.
23. Sigle, D. O.; Zhang, L.; Ithurria, S.; Dubertret, B.; Baumberg, J. J., Ultrathin CdSe in Plasmonic Nanogaps for Enhanced Photocatalytic Water Splitting. *J Phys Chem Lett* **2015,** *6* (7), 1099-1103.
24. Qiu, J.; Zeng, G.; Pavaskar, P.; Li, Z.; Cronin, S. B., Plasmon-enhanced water splitting on TiO2-passivated GaP photocatalysts. *Phys. Chem. Chem. Phys.* **2014,** *16* (7), 3115-3121.
25. Sönnichsen, C., Franzl, T., Wilk, T., von Plessen, G., Feldmann, J., Wilson, O., & Mulvaney, P. , Drastic reduction of plasmon damping in gold nanorods. . *Phys. Rev. Lett.* **2002,** *88*, 077402.
26. Clavero, C., Plasmon-induced hot-electron generation at nanoparticle/metal-oxide interfaces for photovoltaic and photocatalytic devices. *Nat. Photonics* **2014,** *8* (2), 95-103.
27. Manjavacas, A.; Liu, J. G.; Kulkarni, V.; Nordlander, P., Plasmon-Induced Hot Carriers in Metallic Nanoparticles. *ACS Nano* **2014,** *8* (8), 7630-7638.
28. Lee, J.; Mubeen, S.; Ji, X.; Stucky, G. D.; Moskovits, M., Plasmonic Photoanodes for Solar Water Splitting with Visible Light. *Nano Lett.* **2012,** *12* (9), 5014-5019.
29. Knight, M. W.; Sobhani, H.; Nordlander, P.; Halas, N. J., Photodetection with Active Optical Antennas. *Science* **2011,** *332* (6030), 702-704.
30. García de Arquer, F. P.; Mihi, A.; Konstantatos, G., Large-Area Plasmonic-Crystal–Hot-Electron-Based Photodetectors. *ACS Photonics* **2015,** *2* (7), 950-957.
31. Li, W.; Valentine, J., Metamaterial Perfect Absorber Based Hot Electron Photodetection. *Nano Lett.* **2014,** *14* (6), 3510-3514.
32. Mubeen, S.; Lee, J.; Singh, N.; Kramer, S.; Stucky, G. D.; Moskovits, M., An autonomous photosynthetic device in which all charge carriers derive from surface plasmons. *Nat. Nanotechnol.* **2013,** *8* (4), 247-251.
33. Kamat, P. V., Photovoltaics: Capturing hot electrons. *Nat. Chem.* **2010,** *2* (10), 809-810.
34. Shi, Y.; Wang, J.; Wang, C.; Zhai, T.-T.; Bao, W.-J.; Xu, J.-J.; Xia, X.-H.; Chen, H.-Y., Hot Electron of Au Nanorods Activates the Electrocatalysis of Hydrogen Evolution on MoS2 Nanosheets. *J. Am. Chem. Soc.* **2015,** *137* (23), 7365-7370.
35. Kang, Y.; Gong, Y.; Hu, Z.; Li, Z.; Qiu, Z.; Zhu, X.; Ajayan, P. M.; Fang, Z., Plasmonic hot electron enhanced MoS2 photocatalysis in hydrogen evolution. *Nanoscale* **2015,** *7* (10), 4482-4488.

36. Schweikhard, V.; Grubisic, A.; Baker, T. A.; Nesbitt, D. J., Multiphoton Scanning Photoionization Imaging Microscopy for Single-Particle Studies of Plasmonic Metal Nanostructures. *J Phys Chem C* **2011,** *115* (1), 83-91.
37. Schweikhard, V.; Grubisic, A.; Baker, T. A.; Thomann, I.; Nesbitt, D. J., Polarization-Dependent Scanning Photoionization Microscopy: Ultrafast Plasmon-Mediated Electron Ejection Dynamics in Single Au Nanorods. *Acs Nano* **2011,** *5* (5), 3724-3735.
38. Li, J.; Cushing, S. K.; Zheng, P.; Meng, F.; Chu, D.; Wu, N., Plasmon-induced photonic and energy-transfer enhancement of solar water splitting by a hematite nanorod array. *Nat. Commun.* **2013,** *4*.
39. Kim, H. J.; Lee, S. H.; Upadhye, A. A.; Ro, I.; Tejedor-Tejedor, M. I.; Anderson, M. A.; Kim, W. B.; Huber, G. W., Plasmon-Enhanced Photoelectrochemical Water Splitting with Size-Controllable Gold Nanodot Arrays. *ACS Nano* **2014,** *8* (10), 10756-10765.
40. Chen, H. M.; Chen, C. K.; Chen, C.-J.; Cheng, L.-C.; Wu, P. C.; Cheng, B. H.; Ho, Y. Z.; Tseng, M. L.; Hsu, Y.-Y.; Chan, T.-S.; Lee, J.-F.; Liu, R.-S.; Tsai, D. P., Plasmon Inducing Effects for Enhanced Photoelectrochemical Water Splitting: X-ray Absorption Approach to Electronic Structures. *ACS Nano* **2012,** *6* (8), 7362-7372.
41. Sil, D.; Gilroy, K. D.; Niaux, A.; Boulesbaa, A.; Neretina, S.; Borguet, E., Seeing Is Believing: Hot Electron Based Gold Nanoplasmonic Optical Hydrogen Sensor. *Acs Nano* **2014,** *8* (8), 7755-7762.
42. Li, J. T.; Cushing, S. K.; Zheng, P.; Meng, F. K.; Chu, D.; Wu, N. Q., Plasmon-induced photonic and energy-transfer enhancement of solar water splitting by a hematite nanorod array. *Nat. Commun.* **2013,** *4*.
43. Mukherjee, S.; Libisch, F.; Large, N.; Neumann, O.; Brown, L. V.; Cheng, J.; Lassiter, J. B.; Carter, E. A.; Nordlander, P.; Halas, N. J., Hot Electrons Do the Impossible: Plasmon-Induced Dissociation of H2 on Au. *Nano Lett.* **2013,** *13* (1), 240-247.
44. Mukherjee, S.; Zhou, L.; Goodman, A. M.; Large, N.; Ayala-Orozco, C.; Zhang, Y.; Nordlander, P.; Halas, N. J., Hot-Electron-Induced Dissociation of H2 on Gold Nanoparticles Supported on SiO2. *J. Am. Chem. Soc.* **2014,** *136* (1), 64-67.
45. DuChene, J. S.; Sweeny, B. C.; Johnston-Peck, A. C.; Su, D.; Stach, E. A.; Wei, W. D., Prolonged Hot Electron Dynamics in Plasmonic-Metal/Semiconductor Heterostructures with Implications for Solar Photocatalysis. *Angew Chem Int Edit* **2014,** *53*, 7887-7891.
46. Li, Z.; Ezhilarasu, G.; Chatzakis, I.; Dhall, R.; Chen, C.-C.; Cronin, S. B., Indirect Band Gap Emission by Hot Electron Injection in Metal/MoS2 and Metal/WSe2 Heterojunctions. *Nano Letters* **2015,** *15* (6), 3977-3982.
47. Appavoo, K.; Wang, B.; Brady, N. F.; Seo, M.; Nag, J.; Prasankumar, R. P.; Hilton, D. J.; Pantelides, S. T.; Haglund, R. F., Ultrafast Phase Transition via Catastrophic Phonon Collapse Driven by Plasmonic Hot-Electron Injection. *Nano Lett.* **2014,** *14* (3), 1127-1133.
48. Sundararaman, R.; Narang, P.; Jermyn, A. S.; Goddard, W. A.; Atwater, H. A., Theoretical predictions for hot-carrier generation from surface plasmon decay. *Nat. Commun.* **2014,** *5*.
49. Park, J. Y.; Kim, S. M.; Lee, H.; Naik, B., Hot Electron and Surface Plasmon-Driven Catalytic Reaction in Metal-Semiconductor Nanostructures. *Catal Lett* **2014,** *144* (12), 1996-2004.
50. Fang, Z. Y.; Liu, Z.; Wang, Y. M.; Ajayan, P. M.; Nordlander, P.; Halas, N. J., Graphene-Antenna Sandwich Photodetector. *Nano Lett.* **2012,** *12* (7), 3808-3813.

51. Berini, P., Surface plasmon photodetectors and their applications. *Laser Photonics Rev* **2014,** *8* (2), 197-220.
52. Alavirad, M.; Mousavi, S. S.; Roy, L.; Berini, P., Schottky-contact plasmonic dipole rectenna concept for biosensing. *Opt Express* **2013,** *21* (4), 4328-4347.
53. Kang, Y. M.; Gong, Y. J.; Hu, Z. J.; Li, Z. W.; Qiu, Z. W.; Zhu, X.; Ajayan, P. M.; Fang, Z. Y., Plasmonic hot electron enhanced MoS2 photocatalysis in hydrogen evolution. *Nanoscale* **2015,** *7* (10), 4482-4488.
54. Baffou, G.; Quidant, R., Nanoplasmonics for chemistry. *Chem Soc Rev* **2014,** *43* (11), 3898-3907.
55. Wu, K. F.; Rodriguez-Cordoba, W. E.; Yang, Y.; Lian, T. Q., Plasmon-Induced Hot Electron Transfer from the Au Tip to CdS Rod in CdS-Au Nanoheterostructures. *Nano Lett*. **2013,** *13* (11), 5255-5263.
56. Hagglund, C.; Apell, S. P., Plasmonic Near-Field Absorbers for Ultrathin Solar Cells. *J Phys Chem Lett* **2012,** *3* (10), 1275-1285.
57. Qian, K.; Sweeny, B. C.; Johnston-Peck, A. C.; Niu, W. X.; Graham, J. O.; DuChene, J. S.; Qiu, J. J.; Wang, Y. C.; Engelhard, M. H.; Su, D.; Stach, E. A.; Wei, W. D., Surface Plasmon-Driven Water Reduction: Gold Nanoparticle Size Matters. *J. Am. Chem. Soc*. **2014,** *136* (28), 9842-9845.
58. Chalabi, H.; Schoen, D.; Brongersma, M. L., Hot-Electron Photodetection with a Plasmonic Nanostripe Antenna. *Nano Lett*. **2014,** *14* (3), 1374-1380.
59. Sun, K.; Park, N.; Sun, Z.; Zhou, J.; Wang, J.; Pang, X.; Shen, S.; Noh, S. Y.; Jing, Y.; Jin, S.; Yu, P. K. L.; Wang, D., Nickel oxide functionalized silicon for efficient photo-oxidation of water. *Energy Environ. Sc*. **2012,** *5* (7), 7872-7877.
60. Lunkenheimer, P.; Loidl, A.; Ottermann, C. R.; Bange, K., Correlated barrier hopping in NiO films. *Phys. Rev. B* **1991,** *44* (11), 5927-5930.
61. Zhang, H.; Govorov, A. O., Optical Generation of Hot Plasmonic Carriers in Metal Nanocrystals: The Effects of Shape and Field Enhancement. *J Phys Chem C* **2014,** *118* (14), 7606-7614.
62. Scholl, J. A.; Koh, A. L.; Dionne, J. A., Quantum plasmon resonances of individual metallic nanoparticles. *Nature* **2012,** *483* (7390), 421-U68.
63. Ouyang, F.; Batson, P. E.; Isaacson, M., Quantum Size Effects in the Surface-Plasmon Excitation of Small Metallic Particles by Electron-Energy-Loss Spectroscopy. *Phys. Rev. B* **1992,** *46* (23), 15421-15425.
64. Masuda, H.; Fukuda, K., Ordered Metal Nanohole Arrays Made by a Two-Step Replication of Honeycomb Structures of Anodic Alumina. *Science* **1995,** *268* (5216), 1466-1468.
65. Hideki, M.; Masahiro, S., Fabrication of Gold Nanodot Array Using Anodic Porous Alumina as an Evaporation Mask. *Japanese J. Appl. Phys*. **1996,** *35* (1B), L126.
66. Wu, Y.; Cheng, G.; Katsov, K.; Sides, S. W.; Wang, J.; Tang, J.; Fredrickson, G. H.; Moskovits, M.; Stucky, G. D., Composite mesostructures by nano-confinement. *Nat Mater* **2004,** *3* (11), 816-822.
67. Li, J.; Sattayasamitsathit, S.; Dong, R.; Gao, W.; Tam, R.; Feng, X.; Ai, S.; Wang, J., Template electrosynthesis of tailored-made helical nanoswimmers. *Nanoscale* **2014,** *6* (16), 9415-9420.
68. Zhang, A.; Hou, K.; Gu, L.; Dai, C.; Liu, M.; Song, C.; Guo, X., Synthesis of Silica Nanotubes with Orientation Controlled Mesopores in Porous Membranes via Interfacial Growth. *Chemistry of Materials* **2012,** *24* (6), 1005-1010.

69. Lei, Y.; Cai, W.; Wilde, G., Highly ordered nanostructures with tunable size, shape and properties: A new way to surface nano-patterning using ultra-thin alumina masks. *Progress in Materials Science* **2007,** *52* (4), 465-539.
70. Banholzer, M. J.; Qin, L.; Millstone, J. E.; Osberg, K. D.; Mirkin, C. A., On-wire lithography: synthesis, encoding and biological applications. *Nat. Protocols* **2009,** *4* (6), 838-848.
71. Meng, G.; Yanagida, T.; Nagashima, K.; Yanagishita, T.; Kanai, M.; Oka, K.; Klamchuen, A.; Rahong, S.; Horprathum, M.; Xu, B.; Zhuge, F.; He, Y.; Masuda, H.; Kawai, T., Facile and scalable patterning of sublithographic scale uniform nanowires by ultra-thin AAO free-standing membrane. *RSC Advances* **2012,** *2* (28), 10618-10623.
72. Lee, W.; Park, S.-J., Porous Anodic Aluminum Oxide: Anodization and Templated Synthesis of Functional Nanostructures. *Chemical Reviews* **2014,** *114* (15), 7487-7556.
73. Cho, Y., Lee, W., Jhon, Y. K., Genzer, J. and Char, K. , Polymer Nanotubules Obtained by Layer-by-Layer Deposition within AAO-Membrane Templates with Sub-100-nm Pore Diameters. *Small,* **2010,** *6*, 2683-2689.
74. Md Jani, A. M.; Losic, D.; Voelcker, N. H., Nanoporous anodic aluminium oxide: Advances in surface engineering and emerging applications. *Progress in Materials Science* **2013,** *58* (5), 636-704.
75. Tarish, S.; Wang, Z.; Al-Haddad, A.; Wang, C.; Ispas, A.; Romanus, H.; Schaaf, P.; Lei, Y., Synchronous Formation of ZnO/ZnS Core/Shell Nanotube Arrays with Removal of Template for Meliorating Photoelectronic Performance. *The Journal of Physical Chemistry C* **2015,** *119* (3), 1575-1582.
76. H. Masuda, H. A., M. Watanabe, K. Nishio, M. Nakao, T. Tamamura, Square and triangular nanohole array architectures in anodic alumina. . *Adv Mater* **2001,** *13* (3), 189-192.
77. Sun, Z.; Kim, H. K., Growth of ordered, single-domain, alumina nanopore arrays with holographically patterned aluminum films. *Applied Physics Letters* **2002,** *81* (18), 3458-3460.
78. Leung, S.-F.; Gu, L.; Zhang, Q.; Tsui, K.-H.; Shieh, J.-M.; Shen, C.-H.; Hsiao, T.-H.; Hsu, C.-H.; Lu, L.; Li, D.; Lin, Q.; Fan, Z., Roll-to-roll fabrication of large scale and regular arrays of three-dimensional nanospikes for high efficiency and flexible photovoltaics. *Sci. Rep.* **2014,** *4*.
79. Masahiro, H.; Toshiaki, K.; Takashi, Y.; Kazuyuki, N.; Hideki, M., Anodic Porous Alumina Masks with Checkerboard Pattern. *Applied Physics Express* **2010,** *3* (1), 015001.
80. Kustandi, T. S.; Loh, W. W.; Gao, H.; Low, H. Y., Wafer-Scale Near-Perfect Ordered Porous Alumina on Substrates by Step and Flash Imprint Lithography. *ACS Nano* **2010,** *4* (5), 2561-2568.
81. Zhan, Z.; Lei, Y., Sub-100-nm Nanoparticle Arrays with Perfect Ordering and Tunable and Uniform Dimensions Fabricated by Combining Nanoimprinting with Ultrathin Alumina Membrane Technique. *ACS Nano* **2014,** *8* (4), 3862-3868.
82. Lyu, S.-H.; Lee, J.-S., Highly scalable resistive switching memory cells using pore-size-controlled nanoporous alumina templates. *Journal of Materials Chemistry* **2012,** *22* (5), 1852-1861.
83. Geyer, N.; Huang, Z.; Fuhrmann, B.; Grimm, S.; Reiche, M.; Nguyen-Duc, T.-K.; de Boor, J.; Leipner, H. S.; Werner, P.; Gösele, U., Sub-20 nm Si/Ge Superlattice Nanowires by Metal-Assisted Etching. *Nano Letters* **2009,** *9* (9), 3106-3110.

84. Shoso, S.; Yasuhiko, M.; Hiroyuki, S.; Takayuki, T., Formation of Al Dot Hexagonal Array on Si Using Anodic Oxidation and Selective Etching. *Japanese Journal of Applied Physics* **2002,** *41* (3B), L340.
85. Wang, Y. D.; Zang, K. Y.; Chua, S. J., Nonlithographic nanopatterning through anodic aluminum oxide template and selective growth of highly ordered GaN nanostructures. *Journal of Applied Physics* **2006,** *100* (5), 054306.
86. Zeng, Z. H., X; Yin, Z; Li,H; Chen, Y; Li, H; Zhang, Q; Ma, J; Boey, F; Zhang, H. , Fabrication of Graphene Nanomesh by Using an Anodic Aluminum Oxide Membrane as a Template. *Adv. Mater.* **2012,** *24* (30), 4138-4142.
87. Wu, M., Wen, L., Lei, Y., Ostendorp, S., Chen, K. and Wilde, G., Ultrathin Alumina Membranes for Surface Nanopatterning in Fabricating Quantum-Sized Nanodots. *Small* **2010,** *6*, 695–699.
88. Huang, Z., Meng, G., Huang, Q., Chen, B., Zhu, C. and Zhang, Z., Large-area Ag nanorod array substrates for SERS: AAO template-assisted fabrication, functionalization, and application in detection PCBs. *J. Raman Spectrosc.,* **2013,** *44*, 240-246.
89. Tang, H.; Meng, G.; Li, Z.; Zhu, C.; Huang, Z.; Wang, Z.; Li, F., Hexagonally arranged arrays of urchin-like Ag hemispheres decorated with Ag nanoparticles for surface-enhanced Raman scattering substrates. *Nano Res.* **2015,** *8* (7), 2261-2270.
90. Sun, K.; Meng, G.; Huang, Q.; Zhao, X.; Zhu, C.; Huang, Z.; Qian, Y.; Wang, X.; Hu, X., Gap-tunable Ag-nanorod arrays on alumina nanotip arrays as effective SERS substrates. *Journal of Materials Chemistry C* **2013,** *1* (33), 5015-5022.
91. Al Haddad, A.; Zhan, Z.; Wang, C.; Tarish, S.; Vellacheri, R.; Lei, Y., Facile Transferring of Wafer-Scale Ultrathin Alumina Membranes onto Substrates for Nanostructure Patterning. *ACS Nano* **2015**.
92. Hideki, M.; Mitsutaka, N.; Takuya, M.; Kazuyuki, N., Long-Range-Ordered Anodic Porous Alumina with Reduced Hole Interval Formed in Highly Concentrated Sulfuric Acid Solution. *Japanese Journal of Applied Physics* **2006,** *45* (4L), L406.
93. Malinovskis, U.; Poplausks, R.; Apsite, I.; Meija, R.; Prikulis, J.; Lombardi, F.; Erts, D., Ultrathin Anodic Aluminum Oxide Membranes for Production of Dense Sub-20 nm Nanoparticle Arrays. *The Journal of Physical Chemistry C* **2014,** *118* (16), 8685-8690.
94. Han, C. Y.; Willing, G. A.; Xiao, Z.; Wang, H. H., Control of the Anodic Aluminum Oxide Barrier Layer Opening Process by Wet Chemical Etching. *Langmuir* **2007,** *23* (3), 1564-1568.
95. Chen, J., Albella, P., Pirzadeh, Z., Alonso-González, P., Huth, F., Bonetti, S., Bonanni, V., Åkerman, J., Nogués, J., Vavassori, P., Dmitriev, A., Aizpurua, J. and Hillenbrand, R. , Plasmonic Nickel Nanoantennas. *Small* **2001,** *7*, 2341-2347.
96. Solanki, P. R.; Kaushik, A.; Agrawal, V. V.; Malhotra, B. D., Nanostructured metal oxide-based biosensors. *NPG Asia Mater* **2011,** *3*, 17-24.
97. Atwater, H. A.; Polman, A., Plasmonics for improved photovoltaic devices. *Nat Mater* **2010,** *9* (3), 205-213.
98. Green, M. A.; Pillai, S., Harnessing plasmonics for solar cells. *Nat Photon* **2012,** *6* (3), 130-132.
99. Xuming, Z.; Yu Lim, C.; Ru-Shi, L.; Din Ping, T., Plasmonic photocatalysis. *Reports on Progress in Physics* **2013,** *76* (4), 046401.

100. Spinelli, P.; Hebbink, M.; de Waele, R.; Black, L.; Lenzmann, F.; Polman, A., Optical Impedance Matching Using Coupled Plasmonic Nanoparticle Arrays. *Nano Lett*. **2011,** *11* (4), 1760-1765.
101. Nilsson, P. O.; Norris, C.; Walldén, L., The electronic structure of gold studied by photoemission. *Phys kondens Materie* **1970,** *11* (3), 220-230.
102. *Lumerical Solutions, Inc*. *http://www.lumerical.com/tcad-products/fdtd/*.
103. Gelderman, K.; Lee, L.; Donne, S. W., Flat-Band Potential of a Semiconductor: Using the Mott–Schottky Equation. *J. Chem. Educ*. **2007,** *84* (4), 685.
104. Macdonald, J. R.; Kenan, W. R., *Impedance Spectroscopy: Emphasizing Solid Materials and Systems*. Wiley: 1987.
105. Renaud, A.; Chavillon, B.; Le Pleux, L.; Pellegrin, Y.; Blart, E.; Boujtita, M.; Pauporte, T.; Cario, L.; Jobic, S.; Odobel, F., CuGaO2: a promising alternative for NiO in p-type dye solar cells. *Journal of Materials Chemistry* **2012,** *22* (29), 14353-14356.
106. Natu, G.; Hasin, P.; Huang, Z.; Ji, Z.; He, M.; Wu, Y., Valence Band-Edge Engineering of Nickel Oxide Nanoparticles via Cobalt Doping for Application in p-Type Dye-Sensitized Solar Cells. *ACS Appl. Mater. Interfaces* **2012,** *4* (11), 5922-5929.
107. Sato, H.; Minami, T.; Takata, S.; Yamada, T., Transparent conducting p-type NiO thin films prepared by magnetron sputtering. *Thin Solid Films* **1993,** *236* (1–2), 27-31.
108. Chen, H.-L.; Yang, Y.-S., Effect of crystallographic orientations on electrical properties of sputter-deposited nickel oxide thin films. *Thin Solid Films* **2008,** *516* (16), 5590-5596.

Appendix A. Spectrum of the light source

A spectrometer (AvaSpec-2048-USB2) was used to record the spectral output of our solar simulator. The black line shows the output of the solar simulator with an AM1.5 filter installed. The AM1.5 spectrum is plotted as a reference for comparison (red line).

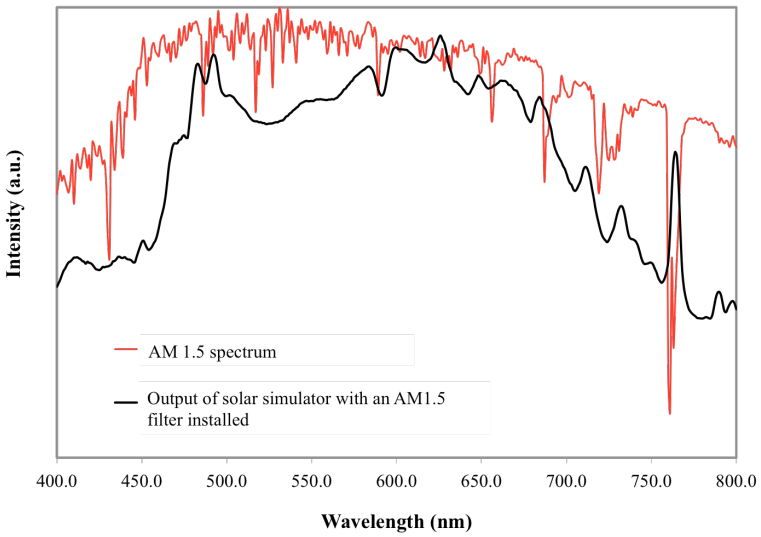

Figure A.1. Spectrum of the light source used for our measurements (black line) compared to AM 1.5 spectrum (red line).

Appendix B: XRD characterization of NiO_x

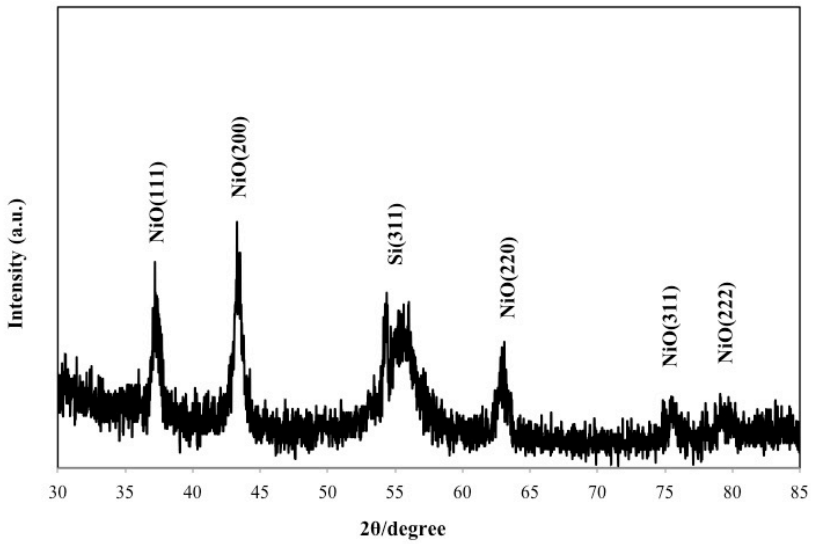

Figure A.2. XRD pattern of NiO_x thin film prepared on a Si substrate. All the diffraction peaks can be indexed face-centered cubic (FCC) NiO_x [7] [8] [9]. A Rigaku SmartLab x-ray diffractometer with Cu x-ray tube was used to obtain the diffraction peaks of a 40nm NiO_x thin film prepared on a Si substrate.

Appendix C: SEM characterization of NiO_x

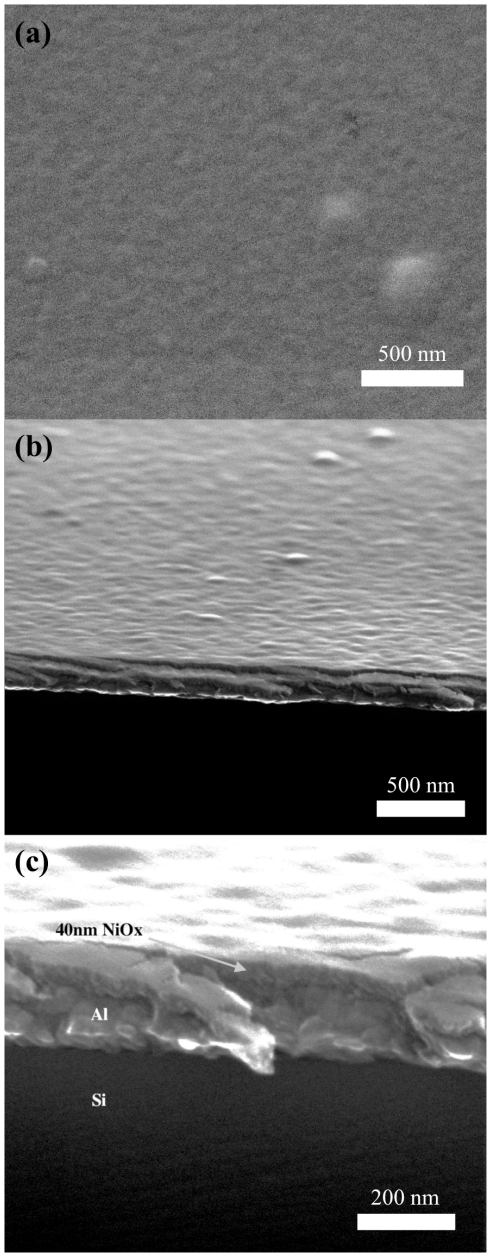

Figure A.3. SEM images of 40nm NiO_x thin film prepared on an Al/Si substrate from NiO_x sol-gel by spin-coating at 4000 rpm for 15 seconds (see fabrication section). According to SEM images the NiO_x film on top of the Al/Si substrate is uniform, smooth and crack-free.

Appendix D: Optical characterization of NiO_x

For optical characterization, a NiO_x thin film with a thickness of approximately 40 nm was prepared on a glass substrate (Corning 2947 Microslide). The monochromated beam with spot size of 3 mm was focused on the sample using a 60 mm plano-convex lens (Thorlabs). The reflected and transmitted light was collected using an IS200 integrating sphere along with a IS236A Silicon photodetector (300 nm to 1100 nm). We measured the optical absorption/transmission spectra within the wavelength range from 300 nm to 700 nm. The transmittance was more than 70% over the entire visible region and reaches up to 90% at 700 nm. Based on the absorption spectra the band gap of NiO_x was calculated to be about 3.45 eV.

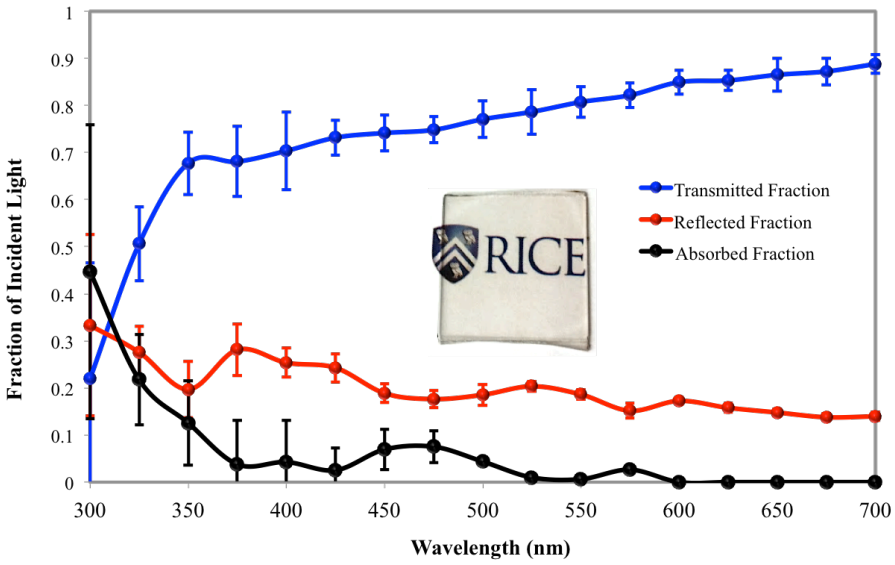

Figure A.4. Optical characterization and corresponding digital image of ~ 40 nm thick NiO_x thin film prepared on top of a glass substrate (Corning 2947 Microslide).

Appendix E: Electrochemical impedance spectroscopy (EIS) characterization of NiO_x

Electrochemical Impedance Spectroscopy (EIS) was performed on the NiO_x sample (without Au nanoparticles). Mott-Schottky (M-S) is a well-known technique to determine the flat band potential and the carrier concentration at the semiconductor-electrolyte interface [103] [104].

An SP-300 potentiostat (Bio-Logic Science Instruments, USA) with LabVIEW version 2011 was used to perform electrochemical impedance spectroscopy on a 40 nm NiO_x thin film prepared on a 200 nm Al/Si substrate, where a Ag/AgCl (in sat. 3.0 M KCl) reference electrode and a Pt mesh counter electrode were used. Measurements were carried out at room temperature with an AC amplitude of 10 mV and a frequency range from 10 Hz to 15 kHz. Nitrogen-purged 0.5 M Na_2SO_4 buffered at pH 5.2 was used as the electrolyte. A negative slope of the Mott-Schottky (M-S) plot was observed at all frequencies confirming the intrinsic p-type nature of the NiO_x thin film. The apparent flat band potentials were estimated from the M-S plot at frequencies higher than 1 KHz at which surface phenomena can be neglected [105]. The apparent flat band potentials vary from 0.00 (3.5 KHz) to 0.16 (34 KHz) w.r.t NHE. This means the valance band of NiO_x, which is typically 0.3 eV below flat band potential, is close to Fermi level of gold. The calculated carrier densities for different frequencies are in the range of 10^{18}-10^{19} cm^{-3} and are of same order of magnitude as the values previously reported for NiO_x films obtained with different fabrication methods [7] [106] [107] [108].

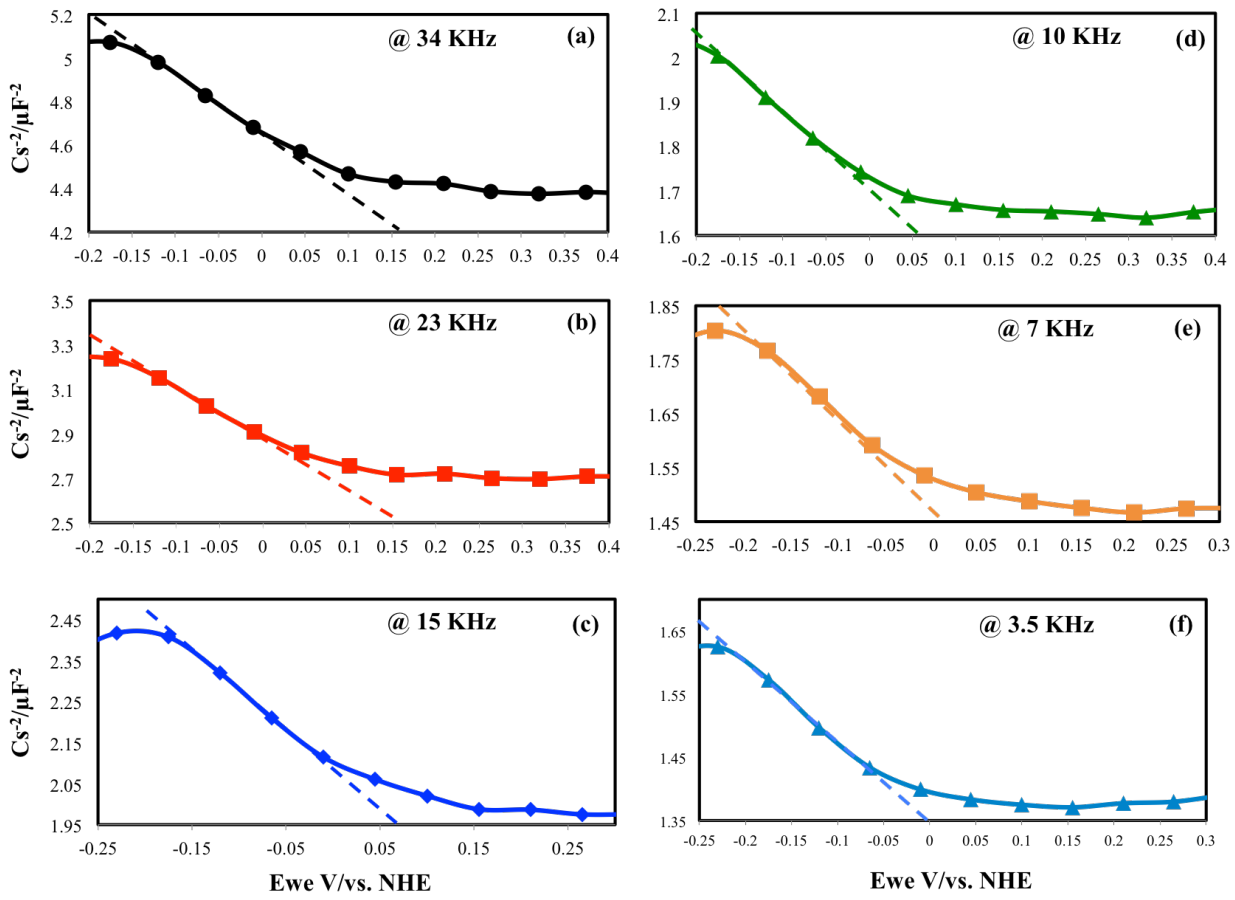

Figure A.5. Mott-Schottky (M-S) plots of 40 nm NiO_x/Al/Si sample acquired at high frequencies above 1 KHz in Nitrogen-purged 0.5 M Na2SO4 buffered at ~ pH 5. The apparent flat band potentials vary from 0.00 (3.5 KHz) to 0.16 (34 KHz) w.r.t NHE. This means the valance band of NiO_x, which is typically 0.3 eV below flat band potential, is close to Fermi level of gold. The calculated carrier densities for different frequencies are in the range of 10^{18}-10^{19} cm^{-3}.